Modeling Environmental Effects on Ventilated Spent Fuel Storage Systems

Spent Fuel and Waste Disposition

Prepared for
U.S. Department of Energy
Spent Fuel and Waste Science and Technology

Pacific Northwest National Laboratory
Ben J. Jensen
Sarah R. Suffield
Megan E. Higley
Brian M. Hom
James A. Fort

September 30, 2021
M3SF-21PN010203025
PNNL-32093

SUMMARY

This report describes newly developed external environment wind effects models of spent nuclear fuel (SNF) dry storage systems. The primary purpose of these wind effects models is to better understand particle deposition on SNF canisters in the context of chloride-induced stress corrosion cracking. The goal of this effort is to further the understanding and improve the wind effects model of the Nuclear Horizontal Modular Storage (NUHOMS®) Advanced Horizontal Storage Module–High Seismic (AHSM-HS) storage system in support of the planned Canister Deposition Field Demonstration (CDFD) project (Durbin et al. 2021, Suffield et al. 2021). The steps in this wind effects investigation begin with a validation case of comparing experimental data with a STAR-CCM+ computational fluid dynamics (CFD) model of the Belowground Vertical Dry Cask Simulator (BVDCS) with the external environment explicitly modeled. Next, a test case is performed with the AHSM-HS models comparing solar-loading strategies for a standalone and wind effects model in STAR-CCM+ and a standalone model in ANSYS Mechanical Parametric Design Language (APDL). The final portion of this study compares results of the validation exercise with applications of wind effects models for two horizontal storage systems, a site specific NUHOMS® horizontal storage module and a NUHOMS® AHSM-HS.

The first portion of this study details a validation case performed on the BVDCS comparing results from a STAR-CCM+ CFD model to experimental data. Although the primary purpose of this research effort is to further develop horizontal SNF dry storage CFD models, little experimental wind effects data is available for horizontal SNF dry storage systems. This set of data for the BVDCS is comprehensive and provides a good example of the effects of crosswinds on a simulated dry cask system (Durbin and Lindgren 2017). The BVDCS model was developed by taking the previous Vertical Dry Cask Simulator (VDCS) STAR-CCM+ model (Suffield et al. 2020a) and adapting it to the belowground configuration to represent the experimental setup detailed in Durbin et al. (2017). Matching crosswind speeds were run in the STAR-CCM+ model and compared to the results from the experimental BVDCS. In addition, a sensitivity analysis using the STAR-CCM+ model was conducted. From this analysis, several sensitive parameters and model improvements were identified. The results of the STAR-CCM+ model matched the trends seen in the experimental measurements. The main conclusion from this validation exercise is the STAR-CCM+ model reproduces the experimental wind effects reasonably well and provides support for further wind effects modeling with STAR-CCM+.

The second portion of this study addresses the implementation of solar radiation in wind effects models. In STAR-CCM+, external environments are handled differently between the standalone module and the wind effects models, which enclose the storage module with an exterior flow region. Solar radiation is modeled differently in each, and there was a question about whether the approach used in the wind effects model would give equivalent and correct results. The approach used in this portion of the study is to use two independent models of the AHSM-HS—one in STAR-CCM+ and the other in ANSYS APDL—to compare the application of solar radiation in each. First, methods of implementing solar radiation between the STAR-CCM+ standalone model with the STAR-CCM+ wind effects model are compared. These two different ways of modeling solar radiation showed very similar exterior temperature profiles and maximum external surface temperatures. The next part compared solar radiation in the standalone simplified AHSM-HS STAR-CCM+ model to the same ANSYS APDL model. The STAR-CCM+ model compared very well to the ANSYS APDL model in both the exterior temperature profile and maximum exterior temperatures. This shows that the STAR-CCM+ method of implementing solar radiation in wind effects models is well understood and matches previous work of implementing solar radiation into standalone models.

The last part of this study provides further insight into previous wind effects modeling with two NUHOMS® systems. One of these is the site-specific HSM design employed at Calvert Cliffs Nuclear Power Plant that was previously modeled (Suffield et al. 2012). The other is for the AHSM-HS model (Suffield et al. 2021). The results from this investigation showed for the limited set of data that the

crosswind response of these systems matched the results of the previously mentioned validation case with the BVDCS and each other. In addition, several model improvements and items for future investigation on the AHSM-HS model were identified.

In conclusion, through these modeling exercises a wind effects STAR-CCM+ model of the BVDCS was validated, several modeling improvements were made, and topics for future investigation were identified. The main objective of this project moving forward is to apply the knowledge gained from this study to the further development of the NUHOMS® AHSM-HS modeling effort to better aid the CDFD project.

ACKNOWLEDGEMENTS

This work was conducted as part of the U.S. Department of Energy (DOE) Spent Fuel and Waste Science and Technology campaign. The authors thank Ned Larson of DOE and Sylvia Saltzstein of Sandia National Laboratories for their support and leadership in this research program.

The authors would also like to thank David Richmond for his review and helpful suggestions and Cary Counts for technical editing.

This page is intentionally left blank.

CONTENTS

LIST OF FIGURES

LIST OF TABLES

This page is intentionally left blank.

ACRONYMS AND ABBREVIATIONS

AHSM-HS	Advanced Horizontal Storage Module – High Seismic
ANL	Argonne National Laboratory
APDL	ANSYS Parametric Design Language
BVDCS	Belowground Vertical Dry Cask Simulator
CDFD	Canister Deposition Field Demonstration
CFD	computational fluid dynamics
CISCC	chloride-induced stress corrosion cracking
CPU	central processing unit
CYBL	Cylindrical Boiling
DSC	Dry Storage Canister
GCI	grid convergence index
HSM	horizontal storage module
ISFSI	Independent Spent Fuel Storage Installation
NRC	U.S. Nuclear Regulatory Commission
NUHOMS®	Nuclear Horizontal Modular Storage
PCT	peak cladding temperature
PDF	probability distribution function
PNNL	Pacific Northwest National Laboratory
SNF	spent nuclear fuel
SNL	Sandia National Laboratories
VDCS	Vertical Dry Cask Simulator

This page is intentionally left blank.

MODELING ENVIRONMENTAL EFFECTS ON VENTILATED SPENT FUEL STORAGE SYSTEMS

1. INTRODUCTION

Pacific Northwest National Laboratory (PNNL) has extensive experience developing thermal models for storage and transportation canisters of spent nuclear fuel (SNF). These models have been mainly for natural convection cases where air flow surrounding the SNF canister is buoyancy driven due to a temperature difference caused by the heat transfer from the SNF canister. To understand the effects of wind on the storage system, initial wind effects models have been developed. The primary focus of studying wind effects is to better understand particle deposition in these SNF dry storage systems, especially as it relates to salt deposition on the surface of the SNF canisters. The deposition of salt on these SNF canisters is a possible precursor to chloride-induced stress corrosion cracking (CISCC). Of interest are aerosols and particles present in a marine environment that are carried by cooling airflows through the storage system. Understanding the extent to which prevailing and episodic wind events influence such deposition is the longer-term goal of this work in support of the Canister Deposition Field Demonstration (CDFD). The CDFD is in the planning stages that will investigate deposition on the canister in an actual storage system (Durbin et al. 2021, Suffield, et al. 2021).

There are few examples of wind effects on SNF storage systems in the literature. The Office of Nuclear Material Safety and Safeguards and the Office of Nuclear Regulatory Research of the U.S. Nuclear Regulatory Commission (NRC) have investigated the impact of wind on the thermal performance of different SNF storage systems in NUREG-2174 (2015). This work focused on the thermal response of the peak cladding temperature (PCT) to wind. In addition to looking at PCT, the PNNL wind effects models also will look at the thermal response of the canister surface to wind. The temperature of a canister is important when considering potential stress corrosion cracking of the canister. Future deposition models will be built from the PNNL thermal models to predict the contaminant deposition on SNF canisters to help aid stress corrosion cracking research. This report focuses on the thermal and flow response of the SNF storage system due to wind effects. Because the PNNL deposition models are built from the thermal models, it is important to validate the thermal and flow model predictions before adding particle deposition.

Validation of models is important to assess accuracy and instill confidence in predicted results. For wind effects on SNF storage systems, a validation study was performed by NRC comparing their model results (NRC 2020) with Sandia National Laboratories (SNL) experimental data on forced flow across the inlet and outlet vents of a simulated underground storage application using the dry cask simulator (Durbin et al. 2017). Although validation experiments for building ventilation applications can be found for both full-scale buildings (Calhoun et al. 2004, 2005) and wind-tunnel models (Van Hooff et al. 2017; Kumar et al. 2021), the SNL dry cask simulator experiment provides the only dataset for a ventilated SNF storage system. For this reason, it also was selected as the validation case in the present study. A validation model was developed, and initial thermal and flow models are presented in this report.

The model validation study is presented in Section 2. This includes a sensitivity study on model parameters. Solar loading is a necessary component of modeling the thermal response of SNF storage systems in an outdoor Independent Spent Fuel Storage Installation (ISFSI). Proposed methods to apply solar loads while modeling the external air flow region around a storage module are described in Section 3. A model comparison is used to validate that approach. The lessons learned modeling approach used in the validation studies were applied in development of a wind effects model from an existing thermal model of a site specific Nuclear Horizontal Modular Storage (NUHOMS®) horizontal storage module. This work is described in Section 4. Following completion of a new thermal model for a NUHOMS® Advanced Horizontal Storage Module – High Seismic (AHSM-HS) system, an external flow field was included to study wind effects. Preliminary results for wind effects models on a single isolated AHSM-

HS module and three connected AHSM-HS modules are shown in Section 5, and development of these models will continue. Future work is recommended to also look at wind effects models for vertical storage systems.

2. MODELING THE BELOWGROUND VERTICAL DRY CASK SIMULATOR WITH CROSSWIND

The purpose of this exercise is to create a STAR-CCM+ model of the Belowground Vertical Dry Cask Simulator (BVDCS) as described in Durbin and Lindgren (2017) and to validate the model results against the experimental results in that same report. Also considered are the computational fluid dynamics (CFD) model results in NRC (2020) which are used as a software-to-software benchmark. The experimental results provide a good dataset to compare against the STAR-CCM+ model results for a variety of different conditions. The focus is to validate the STAR-CCM+ model for SNF storage system models with external environments and “wind driven” crossflows.

Current research efforts are focused on modeling particle deposition on SNF canisters in dry storage. This is important because it will provide insight into the potential for CISCC. It is necessary to model the environment around the SNF storage system to better understand particle deposition in these systems. Previous PNNL models of SNF dry storage systems have not explicitly modeled the external environment and are referred to as standalone models. In these standalone models, the external environment has been represented as an external boundary condition accounting for surface radiation and convection with an external environment temperature. The external convection is calculated using natural convection correlations for different surface geometries. A future objective of this work is to further develop and improve models that explicitly model the external environment surrounding these SNF dry storage systems. This exercise provides a simple example to validate these external environment (wind effects) models with cross flow to improve these external particle deposition models.

2.1 Model Setup

The starting STAR-CCM+ model is the Vertical Dry Cask Simulator (VDCS) used previously in Suffield et al. (2020a) with a few updates and improvements since that model was initially published. These updates include an updated STAR-CCM+ turbulence model, k-effective equations for the porous fuel region, and mesh optimization. With the exception of the turbulence model update, most of the developments were completed during the development of the similar Horizontal Dry Cask Simulator (Suffield et al. 2020b). The original model used the standard k-epsilon low-Reynolds turbulence model. The turbulence model was changed to a k-omega shear stress transport to better account for the increase flows due to the addition of the blower velocity for crosswind testing. The updated model then was configured to match the crosswind testing experimental simulation in Durbin and Lindgren (2017).

2.1.1 Vertical Dry Cask Simulator to Belowground Dry Cask Simulator

To adapt the previous VDCS to the belowground configuration, an outer shell was added. The current VDCS and the updated BVDCS are shown in Figure 2-1 and Figure 2-2, respectively. The four rectangular inlet ducts and flow straighteners are removed, and an insulated outer shell was applied. For the belowground case, the air flows down through the inlets and then up along the canister through the outlet. The airflow path can be seen in Figure 2-3. In the belowground shell, flow straighteners are added to aid in the measurement of the air mass flow through the system. Along with this outer shell, radial inlet and outlet ducts were applied. Figure 2-4 shows a mid-plane radial cross section of the BVDCS with the individual components labeled. Further details about the specifics of the belowground shell and airflow through the cask can be found in Durbin and Lindgren (2017). This standalone BVDCS was used in STAR-CCM+ along with a full model that includes the surrounding environment in the stagnant configuration to establish that the standalone and surrounding environment models are similar.

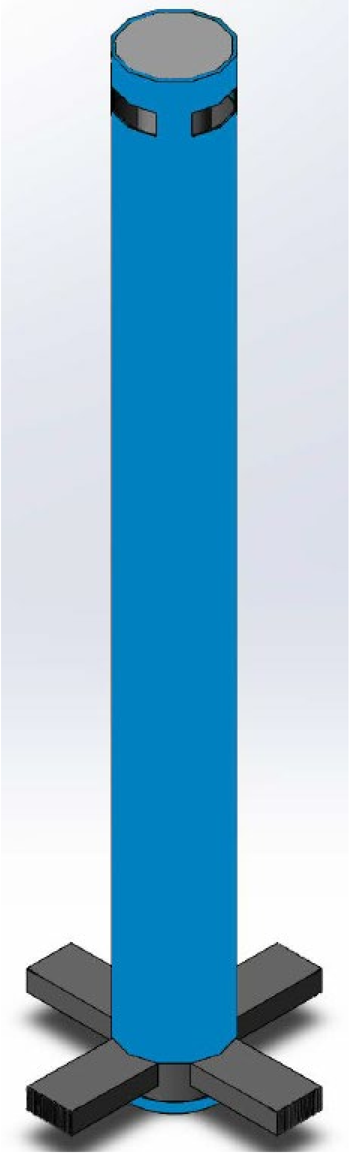

Figure 2-1. Aboveground VDCS

Figure 2-2. BVDCS

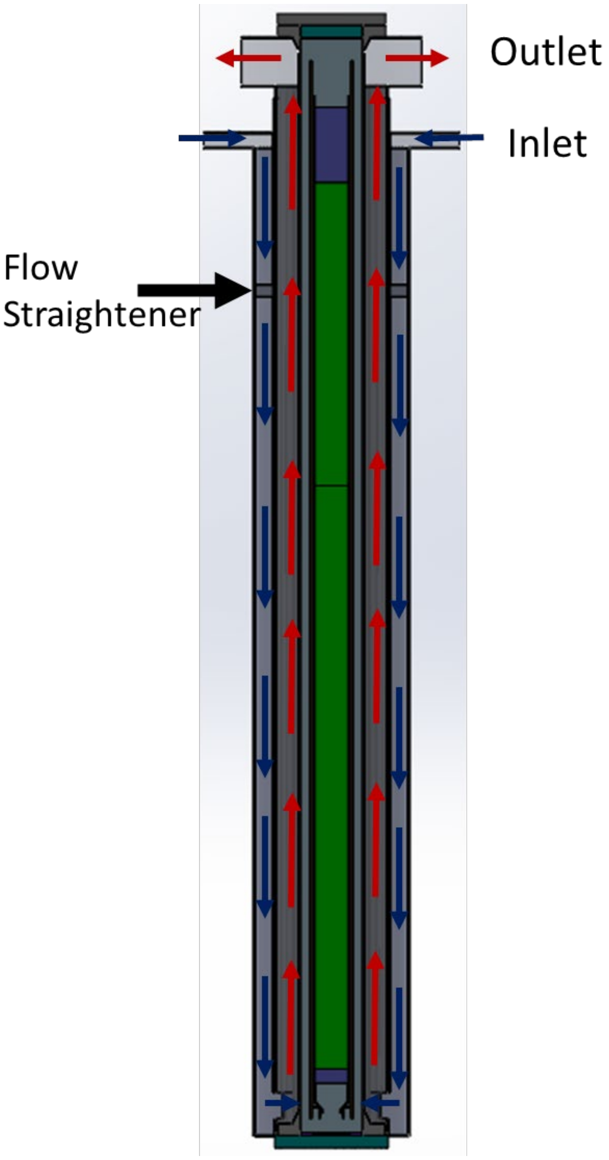

Figure 2-3. Cross Section of the BVDCS Simulator Showing Airflow through the System

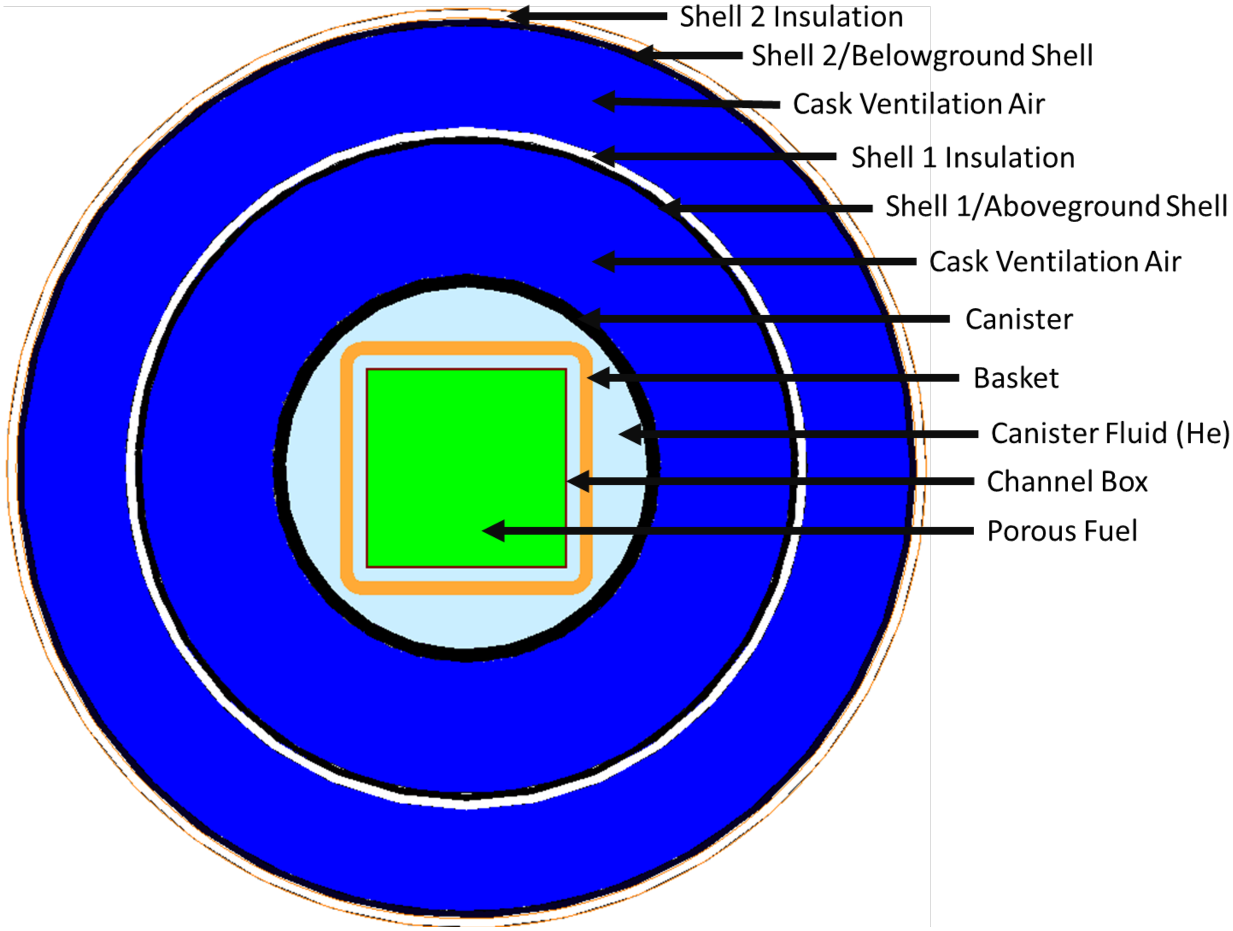

Figure 2-4 Radial cross section of BVDCS with components labeled

2.1.2 CYBL and Wind Machine

To replicate the experiment reported in Durbin and Lindgren (2017), the Cylindrical Boiling (CYBL) system that contains the BVDCS was modeled along with the wind machine. Initially, a simplified model of only the CYBL containment and wind machine was developed as shown in Figure 2-5. This fast-running model was used to test different wind machine geometries and determine necessary blower inlet velocities. The dimensions of the 90° bend, diffuser, blower duct size, and blower duct shape were estimated from images included in Durbin and Lindgren (2017). The diffuser vane and turning vane designs were loosely based on best practices for heating, ventilation, and air conditioning ducting for this CFD model of the wind machine (Modi and Jayanti 2004). There were no design details available for the diffuser and turning vanes in the experimental report (Durbin and Lindgren 2017). The diffuser and turning vanes spread the flow out to match the velocity distribution found in Durbin and Lindgren (2017) for the outlet of the wind machine. The velocities for the three blowers at the top of the wind machine were not specified, only the average velocity at the outlet was presented. This simple model was used in STAR-CCM+ to determine the relationship between the blower velocity and average wind machine outlet velocity. For the final model, this simplified CYBL and wind machine was combined with the BVDCS.

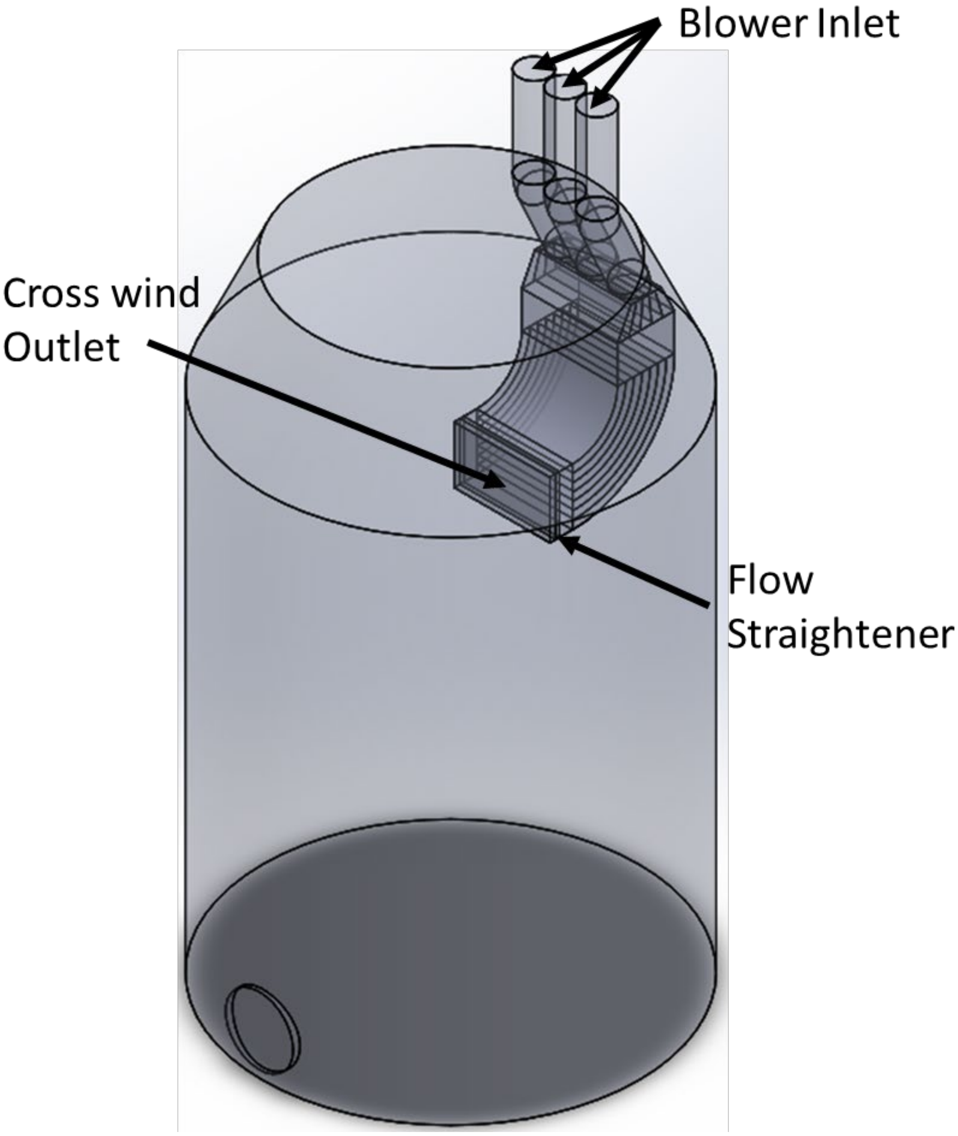

Figure 2-5. CYBL and Wind Machine without the BVDCS

2.1.3 Crosswind Belowground Vertical Dry Cask Simulator

Figure 2-6 shows the full BVDCS with the CYBL and wind machine. This full model was used for the final crosswind model cases and compared to the experimental results. Figure 2-7 shows a full cross section of the BVDCS and CYBL. The top of the CYBL was treated as if it was open so air can escape. The manhole was kept closed for all tests. At the top of the wind machine, a radially uniform velocity was applied to the three openings to represent blowers driving air through the wind machine. For the stagnant tests, the blower inlets were configured as walls to block all airflow from the wind machine, and the top of the CYBL was treated as an open top allowing outflow and inflow due to convection.

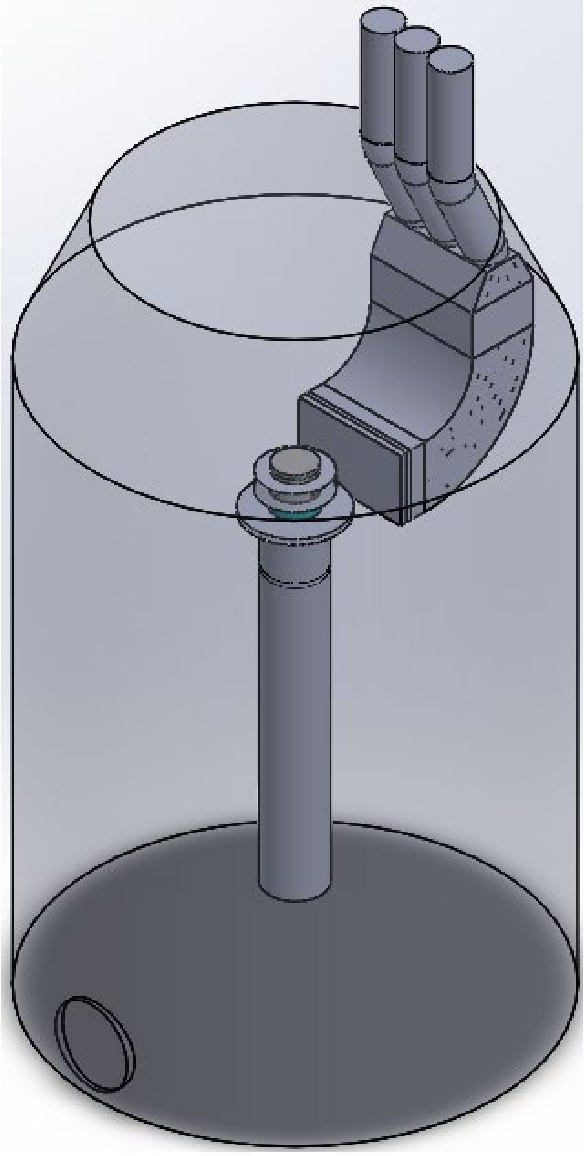

Figure 2-6. BVDCS with CYBL and Wind Machine

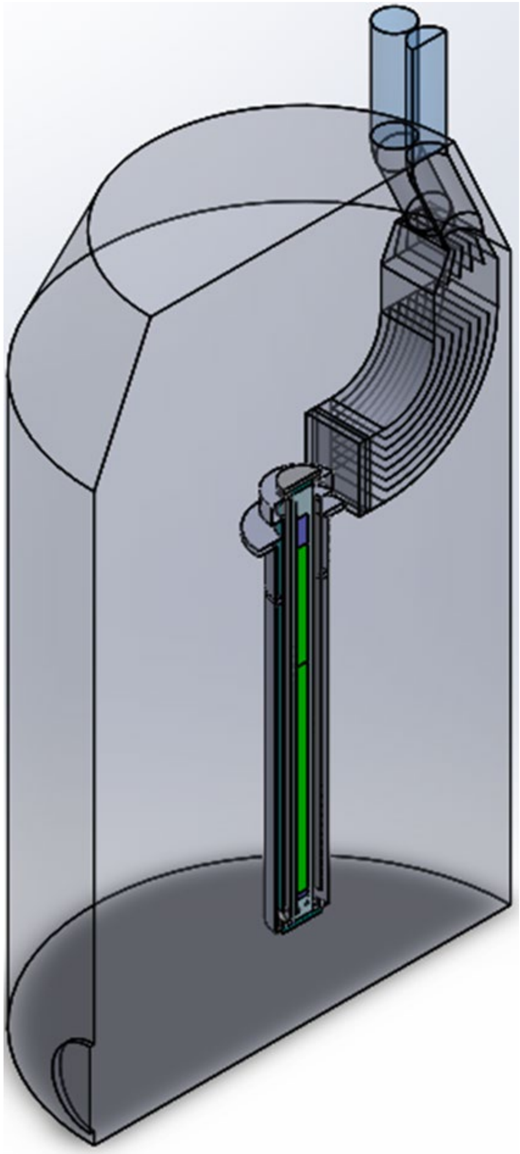

Figure 2-7. Cross section of BVDCS, CYBL, and Wind Machine

2.2 Sensitivity Analysis

To better understand the impact of assumptions made in this modeling effort, a sensitivity analysis was conducted. This sensitivity analysis covered the starting aboveground standalone VDCS, which shares the major components and parameters with the standalone BVDCS, and the BVDCS with the CYBL and wind machine. The aboveground, standalone VDCS and subsequent versions have been used extensively in past studies (Suffield et al. 2020a, 2020b). Several parameters specific to the CYBL and wind machine were included in this study as well. These models were built using many assumptions on uncertain parameters, so it is beneficial to quantify the impacts of these assumptions and uncertainties. In particular, the wind machine ducting was built with little available data in Durbin and Lindgren (2017). This sensitivity analysis is important to improve the validity of this study and to further understand the differences between this CFD modeling effort and the parallel experimental testing on the BVDCS.

The following are some of the many aspects that had to be balanced for the sensitivity studies in this work: computational efficiency, breadth of investigated parameters, mesh considerations, and accurately quantifying uncertainties. To meet these objectives, two models of the VDCS were connected to Dakota, which is SNL-built software with a variety of capabilities including uncertainty quantification and parametric analyses. Dakota facilitates "… design exploration… and quantification of margins and uncertainty with computational models" (Adams et al. 2020). Once Dakota is connected to the simulation software, the user can choose the parameters for perturbation, with the investigated values either chosen by the user or by Dakota for statistical significance. Through connections between Dakota to STAR-CCM+, efficient explorations of the parameter space and uncertainty quantifications of the VDCS models are conducted.

The first analyses were conducted on the standalone aboveground VDCS model, which does not include the CYBL and wind machine. This standalone model is a one-quarter model of the VDCS with symmetry boundary conditions. To investigate the wind effects, models of the CYBL and wind machine are added to the standalone model and the symmetry assumption is removed, so the full 360° geometry was modeled. The standalone model is much more computationally efficient to simulate, so parameters that are not directly tied to the effects of wind are investigated on that model. The parameters found to be sensitive in the stagnant model are assumed to be sensitive in the CYBL wind machine model. Additional analyses were conducted on the CYBL wind machine model to investigate the effect of blower velocity and turbulence on temperatures, which are unique to the CYBL wind machine model. Mesh sensitivity studies were conducted for both models to make sure the heat transfer and flow characteristics are being captured with enough accuracy and the resulting error is estimated. A confidence interval is created for the standalone model and additional uncertainty is added to that confidence interval to account for wind effects. The exploration of both models using a variety of methods helps in the understanding and quantification of uncertainties resulting from a variety of parameters and meshes effectively and efficiently.

2.2.1 Standalone Aboveground VDCS: Parameter Study and Sensitivity Analysis

To narrow down the scope of the sensitivity analysis, a parameter sensitivity study was conducted. In this study, engineering judgement was used to identify 23 parameters that include gap thermal resistances, flow coefficients, material emissivity, effective thermal conductivity values, heat generation rate, ambient temperature, and internal pressure. Table 2.1 lists all 23 parameters. A relative change value was assigned to each of the parameters varying from 50% relative change on the gaps to 5% relative change on the heat generation rate. These relative changes generate a low value and a high value around the original value. For simplicity, all parameters were set to their low values and then increased one-at-a-time to their high value while the PCT is measured as the response variable. The response of each of the variables was calculated with Eq. 1. The change in PCT (ΔPCT) from a perturbed parameter is normalized with the PCT to create a percent change in PCT. This is then compared to the percent change in the parameter, which is the relative change. The parameters with the largest response indicate the parameters with the largest effect on PCT.

$$Response = \frac{\Delta PCT}{PCT * RelativeChange} \tag{1}$$

A plot of these results is shown in Figure 2-8, with the six most sensitive parameters shown in bold in Table 2.1. A sensitive parameter was deemed to have a PCT response greater than +/- 2.5%. Parameters that don't have a visible PCT response plotted in Figure 2-8 had a value less than 0.5%. Power (or heat generation rate) leads to the most significant response in PCT, indicating that its relative change has a significant impact on PCT. Its positive value also indicated a positive relationship, which means that as power increases, PCT increases. This is not true of parameters with negative response values such as helium pressure, because as helium pressure increases, PCT decreases.

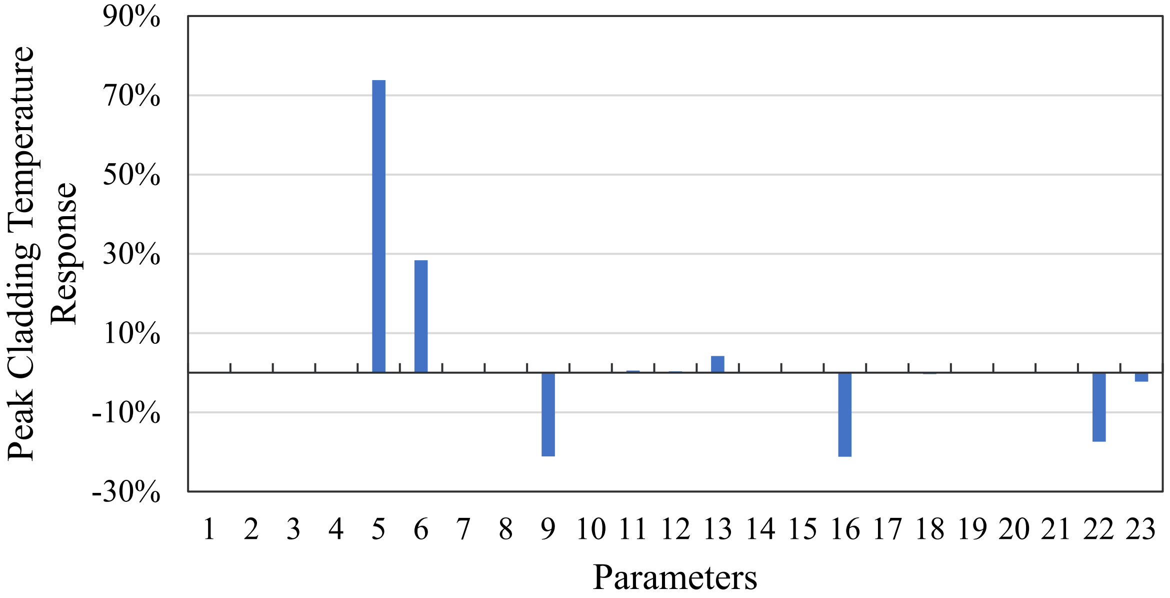

Figure 2-8. Parameter Study Response Results for Each of the 23 Investigated Parameters (parameters with no visible PCT response have values less than 0.5%)

Table 2.1. Parameter Value and Name (Parameters with Largest Responses to PCT shown in bold)

Parameter Value	Parameter Name
1-4	Contact Resistances
5	**Power**
6	**Ambient Temperature**
7-8	Assembly Base Boundary Condition Parameters
9	**Helium Pressure**
10-11	Axial Inertial Flow Coefficients for Porous Regions
12	Axial Porous Viscous Coefficient Flow Straightener
13	**Axial Porous Viscous Coefficient Fuel**
14	Solid Thermal Conductivity for Flow Straightener
15	Emissivity of Concrete
16	**Emissivity Carbon Steel**
17-19	Emissivity of Other Components
20	Axial Effective Thermal Conductivity of Fuel
21	Radial Effective Thermal Conductivity of Full Rod Fuel Region
22	**Radial Effective Thermal Conductivity of Partial Rod Fuel Region**
23	Emissivity of Zircaloy

Parameters with a response of above 2.5% were chosen as sensitive parameters for further investigation into how their relative change affect PCT uncertainty. The sensitive parameters are shown in bold in Table 2.1.

2.2.2 Standalone Aboveground VDCS: Uncertainty Quantification

From the parameter study in Section 2.2.1, heat generation rate, ambient temperature, internal (helium) pressure, the axial porous viscous coefficient, emissivity of carbon steel, and effective thermal conductivity in the radial direction of the partial rod fuel region were determined to be the most sensitive parameters (Table 2.1). The experimental uncertainties of the measurements were found and assigned for the power, ambient temperature, helium pressure, and emissivity (Durbin and Lindgren 2017). An uncertainty of 10% was applied for the viscous coefficient and effective thermal conductivity as they were derived properties. The 10% value was arbitrarily assigned. It is important to note that the results are preliminary and the purpose of the sensitivity study and uncertainty analysis presented in this report was to set up a method for conducting these analyses in the future.

A Latin Hypercube Sampling method with 250 samples was conducted within the uncertainty bounds of each parameter. The uncertainty profiles were assumed to be uniform. The PCT was used as the response parameter, and Dakota calculated the overall mean, overall standard deviation, and the 95% confidence interval high and low means and standard deviation, which removes the assumption of symmetry. As shown in Figure 2-9, a probability distribution function (PDF) was calculated along with the 95% limits. The 95% limits are calculated based on the confidence interval mean +/- the standard deviation multiplied by 2 (a value of 2 was used in place of the standard 1.96 value used for a 95% limit). The experimental measurement is shown in Figure 2-8 with error bars representing its 1% measurement uncertainty.

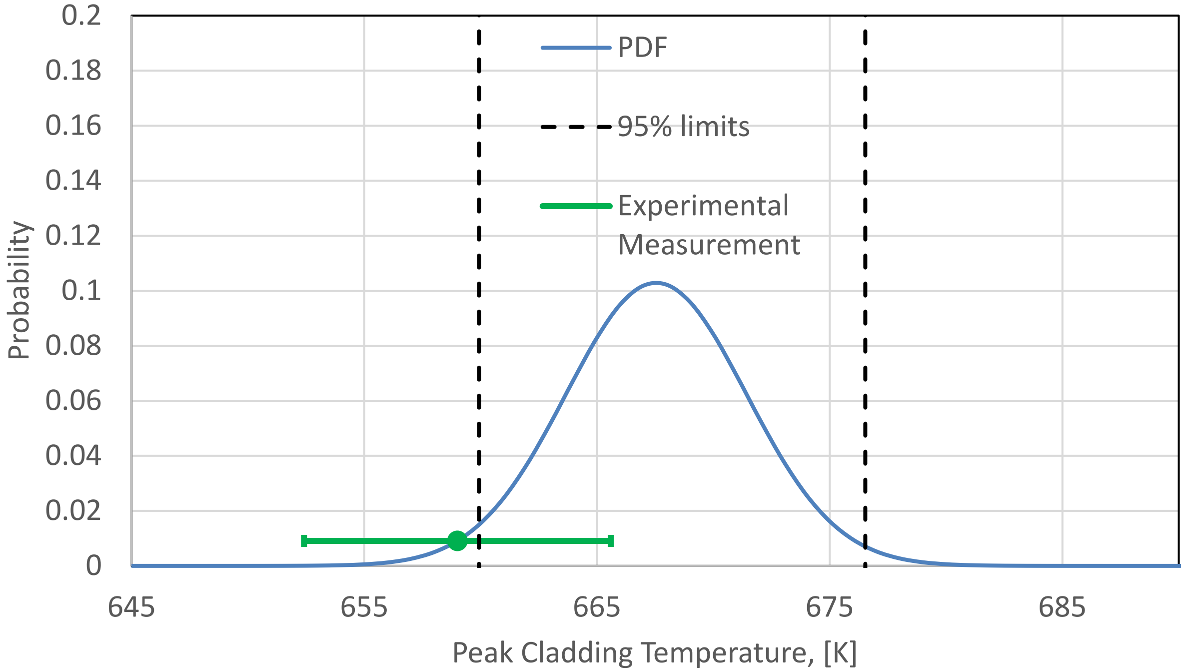

Figure 2-9. Probability Distribution Function, Confidence Interval, and Experimental Measurement of the PCT in the VDCS Derived from Experimental Uncertainties for the 5-kW, 800-kPa Case

The Latin Hypercube Sampling indicates that the peak cladding temperature is between 660 K and 677 K for the 800-kPa and 5-kW standalone case. This 95% limit agrees with experimental data when experimental uncertainty is considered.

2.2.3 BVDCS CYBL and Wind Machine: Wind Speed and Turbulence Sensitivities

For the CYBL wind machine models, the wind speed and turbulence were the parameters of interest because other parameters already had been sampled in the standalone models. Turbulence is a difficult parameter to characterize and model, but an understanding of its effect on temperature prediction is needed. Turbulence was controlled with turbulence intensity and turbulent viscosity. Turbulent viscosity is a flow property for the connection between turbulent stress and the strain of the fluid (Jiang et al. 2020). Turbulence intensity is a parameter related to the deviations in flow from the average, which are characteristic of turbulent flows (Russo and Basse 2016). Flows with 1% turbulence intensity are considered low while a turbulence intensity of 10% are considered high. For this sensitivity, because the turbulence parameters and then blower velocity are not independent, a full factorial study was performed with two levels of treatment per parameter. Blower velocity was 2.5 or 5 m/s, turbulent viscosity ratio was 1 or 20, and turbulence intensity was 0.1% or 10%. Standard values for turbulent viscosity and turbulence intensity are 10% and 1% for reference. This study was done in combination with the mesh sensitivity, discussed below, but for reporting purposes, the results presented are for the fine mesh, tight convergence. Table 2.2 shows the ordered results of these runs. There is no effect of turbulence within the 2.5 m/s velocity block and very little effect of turbulence within the 5 m/s velocity block. Having a lesser effect of turbulence at lower velocities is expected because there is less total flow. Within the 5 m/s velocity block, turbulence intensity has a larger effect at lower turbulent viscosity ratios. Collectively, these results indicate that PCT is more sensitive to blower velocity than turbulence measures, with turbulence having a larger effect at higher velocities.

Table 2.2. Turbulence and Velocity Sensitivity Results for the CYBL Wind Machine Model

Run	Blower Velocity [m/s]	Turbulent Viscosity Ratio	Turbulence Intensity	PCT [K]
1	2.5	1	0.1%	495.9
2	2.5	1	10.0%	495.9
3	2.5	20	10.0%	495.9
4	2.5	20	0.1%	495.9
5	5	1	10.0%	497.5
6	5	20	0.1%	497.7
7	5	20	10.0%	497.7
8	5	1	0.1%	497.8

2.2.4 Mesh Sensitivity and Convergence Criteria

A mesh sensitivity study and a convergence criteria investigation were conducted to better approximate numerical error. The standalone aboveground VDCS model was used for a mesh sensitivity study to look at how element size impacts the PCT. Meshes with smaller element sizes will have a higher element count but will provide more accurate PCT predictions. The trade off with accuracy is computation efficiency, a mesh with less elements will run faster. A smaller, or coarser, mesh will have less elements. The base element size, minimum surface size, and the number of prism layers were used to adjust the mesh using Dakota. The model was meshed after implementing the new parameters and a simulation was run. PCT, cell quality, average wall Y+, element count, solver central processing unit (CPU) time, and number of iterations were the response variables. The wall Y+ value is a non-dimensional distance that indicates how coarse or fine a mesh is in the boundary layer near a wall. A fine mesh near the wall results in lower wall Y+ values. Thirty-four total meshes were run and grid convergence index (GCI) was calculated (Stern et al. 2001). Figure 2-10 shows the raw data from the mesh sensitivity studies. The vast majority of the meshes (33 of the 34) show reasonable PCT predictions within 5 K of the others, even for relatively low mesh counts. One mesh has a significantly different temperature prediction, which can be attributed to its extremely high wall Y+ value of 3.7.

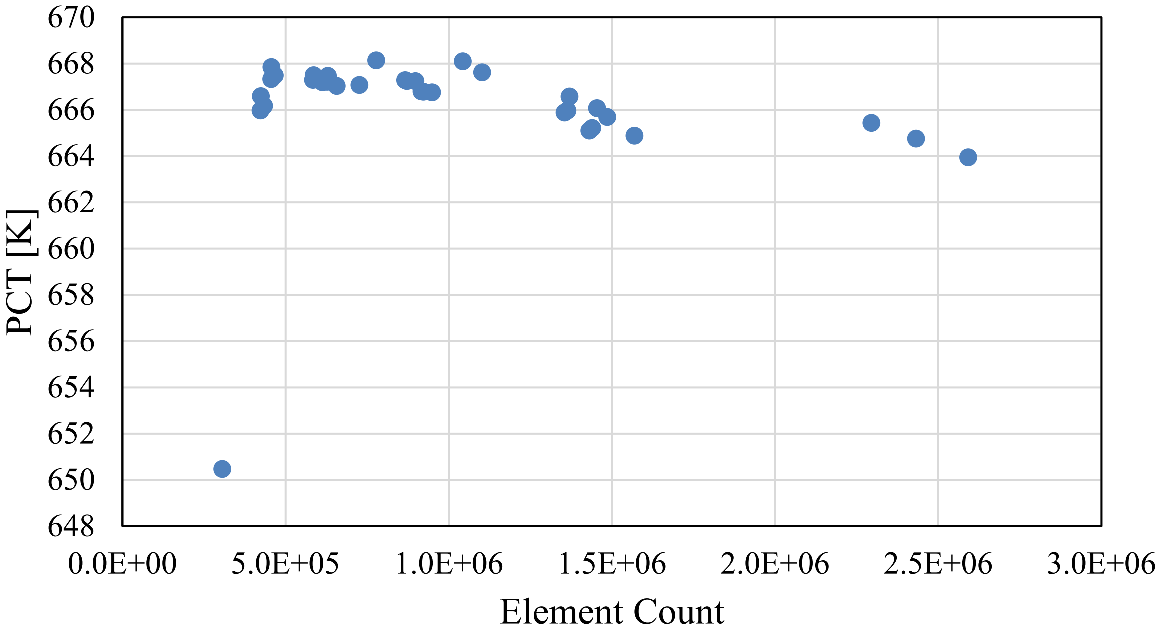

Figure 2-10. PCT Versus Element Count for the Standalone Model Meshes

Using this study, the 34 cases were trimmed down to 9 cases by removing the outlier case from the raw data, including meshes with Y+ values above 1, and removing meshes with CPU times above 80,000 seconds. A GCI was calculated (Stern et al. 2001) on the 9 acceptable meshes. The list of acceptable meshes is shown in Table 2.3. Figure 2-10 shows that the most refined mesh had a cell count around 2,600,000 elements and a PCT of 664 K. This case was used as the baseline mesh for GCI calculations. The estimated error in Table 2.3 is relative to the baseline mesh. Mesh number 2 was used for the previous standalone analysis with an estimated error of 3.9 K. The results show that the estimated error varied from around 2-4 K. Since all the meshes in Table 2.3 had a PCT of around 667 K, which is 3 K above the baseline mesh value of 664 K, the estimated error seems reasonable. It should be noted that the meshes in Table 2.3 had cell counts less than 1.0E6 to get to a CPU time below 80,000 seconds. Future models may want to increase the element count to around 1.6E6 to reduce the estimated error based on the PCT predictions in Figure 2-9. The mesh sensitivity exercise presented provides a method for conducting such analyses with Dakota.

Table 2.3. Acceptable Meshes Based on the GCI, Y+, PCT, and CPU Criteria.

Mesh	Base Size	Minimum Surface Size	Prism Layers	PCT [K]	Elements	GCI	Estimated Error [K]
1	0.25	4	2	667.24	8.98E+05	0.0034	2.2
2	0.25	5	2	667.25	8.72E+05	0.0058	3.9
3	0.25	6	2	667.28	8.66E+05	0.0058	3.9
4	0.25	5	3	666.78	9.22E+05	0.0054	3.6
5	0.25	6	3	666.80	9.17E+05	0.0054	3.6
6	0.25	4	3	666.76	9.49E+05	0.0055	3.7
7	0.3	5	3	667.47	6.30E+05	0.0038	2.5
8	0.3	6	3	667.21	6.28E+05	0.0039	2.6
9	0.3	4	3	667.04	6.57E+05	0.0039	2.6

Because of its prohibitively large mesh size, a much smaller mesh sensitivity was conducted for the CYBL wind machine BVDCS models. Mesh refinement may directly impact how flow is realized so the first portion of the mesh sensitivity checked if there was some effect of blower velocity impacting the necessary mesh size. The results shown in Table 2.4 indicate that there are significant differences between the meshes with the smaller (coarse) mesh predicting a slightly higher PCT. The smaller mesh also predicts larger effects due to blower velocity than the more refined mesh. A potentially confounding factor, however, may have been the iterations to convergence. About half as many iterations were required to reach convergence in the coarse mesh (mesh 2) than the refined mesh (mesh 1). The criterion for convergence of this initial sensitivity was that once the PCT was changing by less than 0.01 K, measured over 10 iterations, the simulation had converged. This small change would indicate that PCT was no longer increasing or decreasing at a significant rate, and it is assumed to be at steady state.

Table 2.4. Initial Mesh Sensitivity of CYBL Wind Machine Model

Mesh	Blower Velocity (m/s)	Base Size (m)	Minimum Surface Size (% of base size)	Prism Layers	PCT (K)	Elements	Iterations
1	2.5	0.2	3	4	708.0	4.50E+07	1830
1	5	0.2	3	4	708.7	4.50E+07	1879
2	2.5	0.25	5	2	712.9	1.50E+07	990
2	5	0.25	5	2	714.4	1.50E+07	971

To further investigate this behavior, more mesh sensitivities were run that also sought to account for convergence criteria and turbulence. The convergence criterion was increased to 0.001 K over 10 iterations, and turbulence was perturbed as described in the turbulence sensitivity. The results are shown in Figure 2-11 for number of iterations versus PCT. Figure 2-11 plots the variation in mesh refinement and turbulence intensity. Increasing the convergence criterion had little impact on increasing the number of iterations to convergence, with it only increasing the number of iterations required by an average of approximately 200 for the coarse mesh and 100 for the fine mesh. The most notable differences between the meshes is the spread of the coarse mesh compared to the refined mesh. The refined mesh offers much more consistent results, even as it accounts for turbulence intensity. The coarse mesh results, however, are spread over a much larger area.

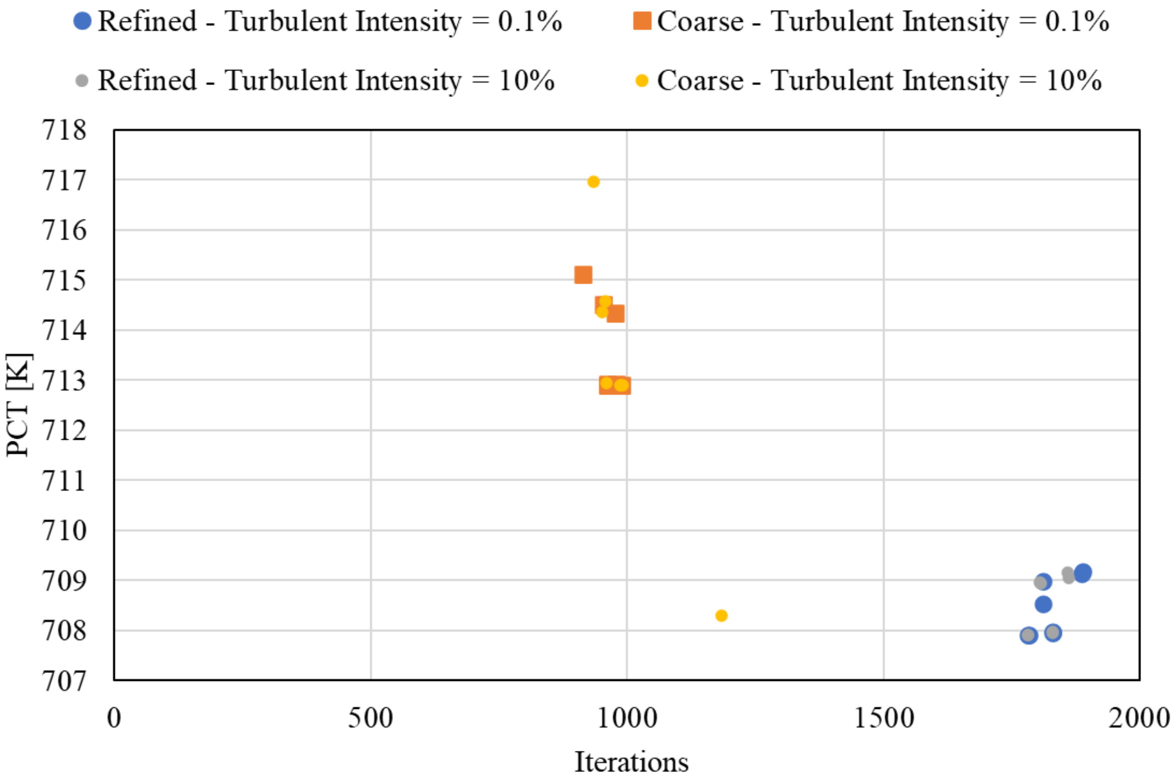

Figure 2-11. Mesh Sensitivity Analysis of the CYBL Wind Machine Models with Turbulence and Convergence Criteria Considerations

2.2.5 Sensitivity and Uncertainty Quantification Summary and Conclusions

Parameter studies, uncertainty quantification, mesh sensitivities, and convergence investigations were completed on models of the VDCS. The parameters found to be sensitive on the standalone aboveground VDCS model, including power and helium pressure, were further investigated on the BVDCS model using a Latin Hypercube Sampling method to calculate the propagation of uncertainty in the measured quantities to the uncertainty in the measurement of PCT. These results were compared to experimental results and found to be in good agreement. Blower velocity and turbulence were investigated on the CYBL wind machine model of the BVDCS and turbulence was found to have a larger effect at higher blower velocities, however, the effect of blower velocity was found to be more significant that turbulence. Mesh discretization were investigated for both models with additional investigation into convergence criteria for the CYBL wind machine model. For the CYBL wind machine model, tighter convergence criteria for the coarse mesh are able to resolve some of the errors resulting from the mesh. The coarser mesh (mesh 2) is used for the final results presented in the next section. This sensitivity and uncertainty quantification provides further insight into the significance of the final results and helps to guide future investigation into these external wind effects models. The sensitivity studies and uncertainty quantification methodology presented in this report will be used for future analyses.

2.3 Results

2.3.1 Stagnant Comparisons

Table 2.5 through Table 2.7 show the results for the initial stagnant modeling effort. Table 2.8 shows the differences between the full STAR-CCM+ model with the CYBL and the experimental results. At all three power levels, the STAR-CCM+ models compared well with the experimental results. The maximum temperature difference for the maximum cladding temperatures is about 3K. For the 5.0 kW heat load case, the maximum temperature of the vessel (canister) is quite a bit different with about 18K difference between the STAR-CCM+ model and experiment. These temperatures for both the experimental and STAR-CCM+ models are measured at the thermocouple locations as described in Durbin and Lindgren (2017). The model updates for this modeling effort from Suffield et al. (2020b) and Suffield et al. (2020a) provide a much better cladding temperature comparison to the dry cask simulator experimental results.

Table 2.6 and Table 2.7 compare the STAR-CCM+ results of the standalone model to the model that includes the CYBL and wind machine. The cladding temperatures are identical. There is a slight difference at the 5.0 kW heat load for some of the other components with the canister vessel being the most significant at a 3K difference. The difference between these two STAR-CCM+ models is negligible, which shows they are both identical for all intents and purposes. This supports the verification of this new model with the CYBL and wind machine developed for this application.

Figure 2-12 and Figure 2-13 show cross sectional profiles of axial velocity and temperatures of the STAR-CCM+ model with the CYBL. As shown in Figure 2-13, there is a significant amount of natural convection from the BVDCS. Most of the air flows from the center of the CYBL with slight recirculation around the edges of the open top. Figure 2-14 shows the velocity magnitude of the air flow through the outer shell of the BVDCS. This cross section was taken at the same axial level as in Durbin and Lindgren (2017) and compares with the same experimental profiles presented in that report.

Table 2.5. Stagnant Experimental Maximum Thermocouple Temperature Results for BVDCS

Case	Cladding (K)	Channel (K)	Basket (K)	Vessel (K)	Shell 1 (K)	Shell 2 (K)	Air Flow (kg/s)
0.5kW, 100kPa	374	358	343	327	310	299	2.64E-02
1.0kW, 100kPa	433	403	378	349	321	301	3.61E-02
5.0kW, 100kPa	704	624	556	473	394	313	6.99E-02

Table 2.6. Stagnant Standalone STAR-CCM+ Model Maximum Thermocouple Temperature Results

Case	Cladding (K)	Channel (K)	Basket (K)	Vessel (K)	Shell 1 (K)	Shell 2 (K)	Air Flow (kg/s)
0.5kW, 100kPa	377	360	348	332	312	299	2.66E-02
1.0kW, 100kPa	436	407	386	358	324	301	3.46E-02
5.0kW, 100kPa	702	627	563	489	404	315	6.92E-02

Table 2.7. Stagnant CYBL and Wind Machine STAR-CCM+ Model Maximum Thermocouple Temperature Results

Case	Cladding (K)	Channel (K)	Basket (K)	Vessel (K)	Shell 1 (K)	Shell 2 (K)	Air Flow (kg/s)
0.5kW, 100kPa	377	360	348	333	312	299	2.55E-02
1.0kW, 100kPa	436	407	386	359	325	301	3.47E-02
5.0kW, 100kPa	702	627	564	491	405	316	6.79E-02

Table 2.8. Difference between the Full STAR-CCM+ Model and Experimental Results

Case	Cladding (K)	Channel (K)	Basket (K)	Vessel (K)	Shell 1 (K)	Shell 2 (K)	Air Flow (kg/s)
0.5kW, 100kPa	3	2	5	6	2	0	-9.34E-04
1.0kW, 100kPa	3	4	8	10	4	0	-1.39E-03
5.0kW, 100kPa	-2	3	8	18	11	3	-2.03E-03

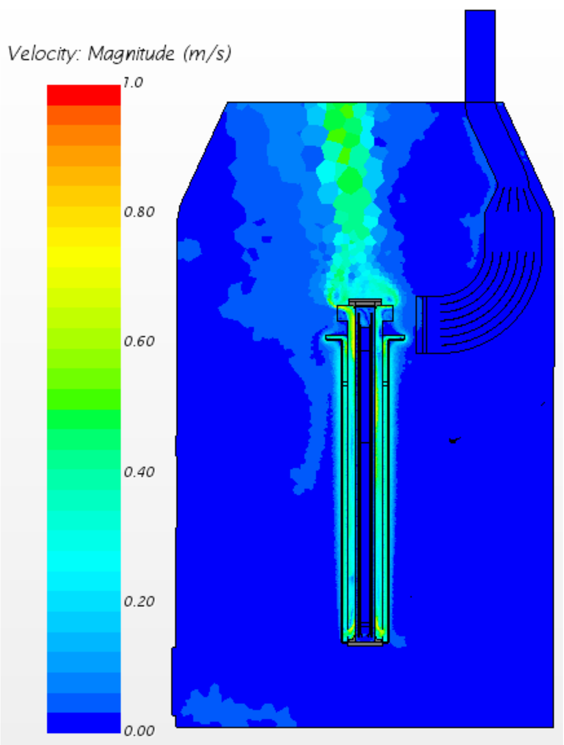

Figure 2-12. Axial Air Velocity Profile of STAR-CCM+ Model with 1.0kW and 100kPa Helium

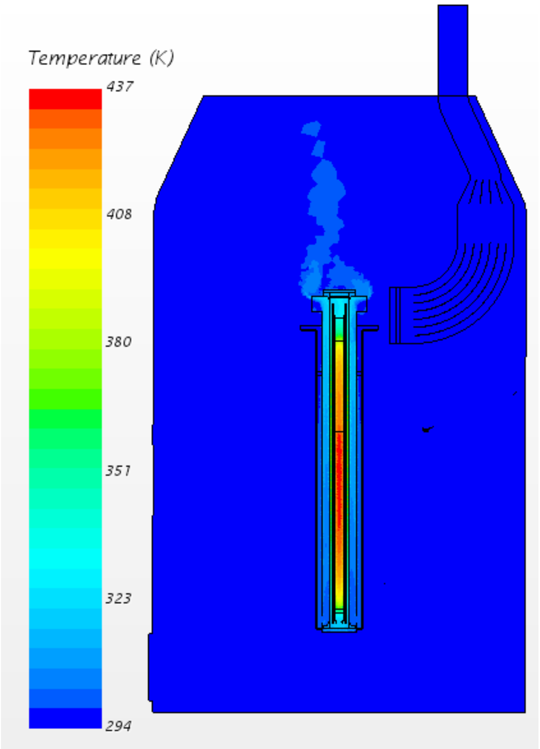

Figure 2-13. Axial Temperature Profile of STAR-CCM+ Model with 1.0kW and 100kPa Helium

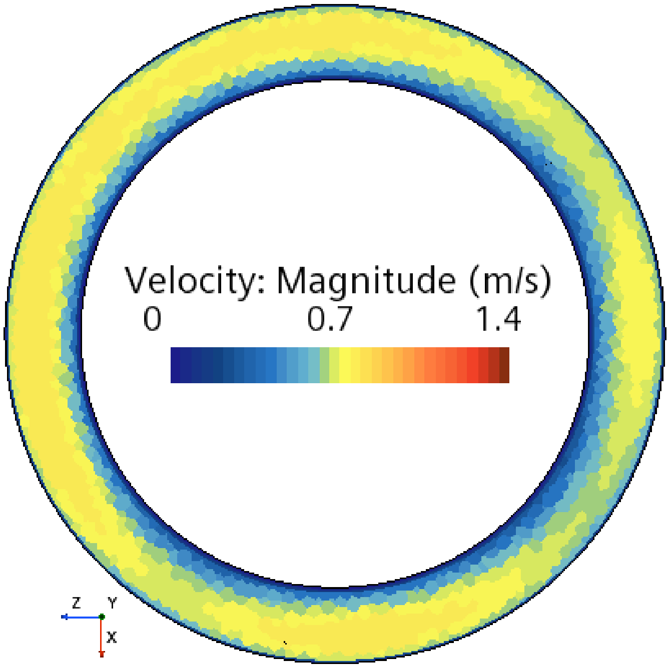

Figure 2-14. 5kW, 100kPa Stagnant Cross Wind, Air Flow Through Belowground Shell

2.3.2 Wind Machine Blower Speed and Outlet Velocity Test Results

To determine the relationship between blower speed and wind machine outlet duct velocity, a set of blower speeds was analyzed, and various points of the outlet duct were measured. The results of these tests are shown in Table 2.9. In the experiment, the “crosswind speed” was measured using the three anemometer points depicted in Figure 2-15. This wind velocity profile was interpolated from the black points that signify hot wire anemometer measurement locations. The black dots were used only once to get a profile of the wind machine outlet velocities at the indicated average crosswind velocity (Durbin and Lindgren 2017).

To better understand the decision to use three points to determine the wind machine outlet velocity, the velocities of each measurement point along with the surface average velocity are included in Table 2.9. Locations of the three points in the STAR-CCM+ model are the same as in the experimental setup. One advantage of CFD analysis is that it is very easy to evaluate specific aspects of the model such as surface velocity of the wind machine outlet, which is a more involved task to evaluate in an experiment. Figure 2-16 shows the wind machine outlet crosswind velocity profile from the STAR-CCM+ CFD model. The difference between the surface average velocity and point average velocity is less than 5% from each other. There is a significant difference between the velocity at point three and point one. This is due to the air velocity at the top of the duct being slower than at the bottom due to the curvature of the duct. This is evident in both the experimental wind machine velocity profile in Figure 2-15 and the STAR-CCM+ model wind velocity profile in Figure 2-16. The variation in the STAR-CCM+ wind machine outlet velocity profile is more pronounced than the experimental profile. The point average velocities are used to determine the blower velocities to match the crosswind speeds tested in the experiment.

Table 2.9. Results of Blower Velocity Test Preformed in STAR-CCM+

Blower Velocity (m/s)	Surface Average Velocity (m/s)	Point Average Velocity (m/s)	Pt 1 Velocity (m/s)	Pt 2 Velocity (m/s)	Pt 3 Velocity (m/s)	Outlet Surface Max Velocity (m/s)
1	0.39	0.39	0.40	0.41	0.37	0.43
5	1.94	1.98	2.05	2.20	1.67	2.53
10	3.87	4.06	4.60	4.40	3.19	5.35
13.5	5.23	5.49	6.30	6.01	4.15	7.08
15	5.81	6.00	6.87	6.57	4.57	7.76
25	9.69	9.94	11.50	10.83	7.50	13.49
50	19.36	20.06	23.56	22.15	14.46	26.74

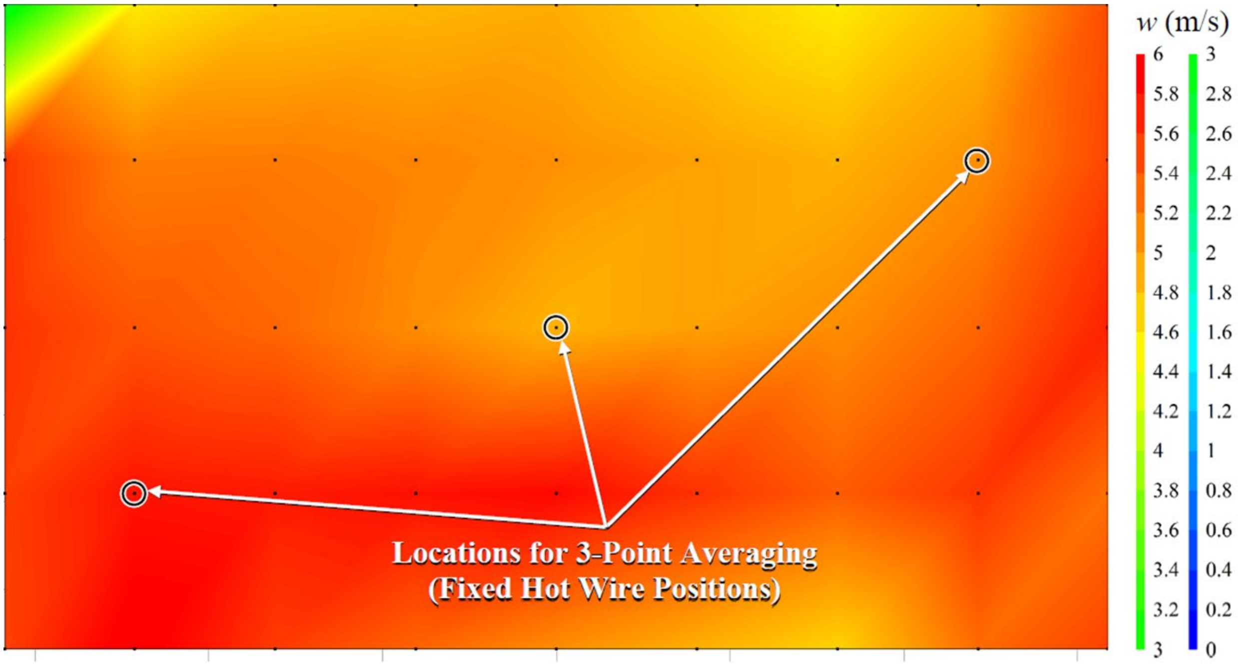

Figure 2-15. Wind Machine Outlet Profile from the Experimental Runs for an Average Velocity of 5.3 m/s (Durbin and Lindgren 2017)

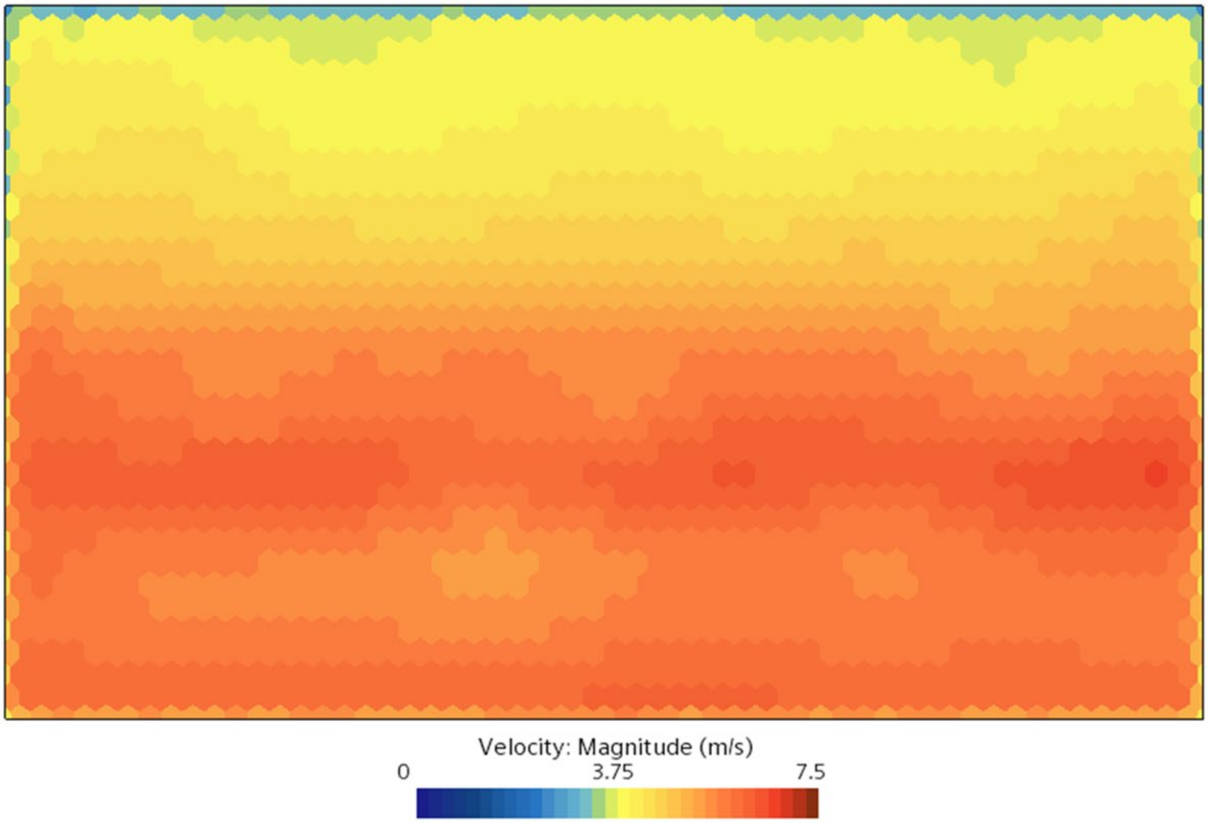

Figure 2-16. STAR-CCM+ Model Wind Machine Outlet Velocity Profile for an Average Crosswind Speed of 5.3 m/s

2.3.3 Crosswind Results and Comparison to Experiment and NRC modeling

Table 2.10 through Table 2.12 show the results of the steady state crosswind tests for the cases analyzed. Included in these tables are the change in PCT from the stagnant case as well as normalized mass flowrate. Because of the increased complexity of experimental setup for the crosswind cases, only two heat loads—1.0kW and 5.0kW—at 100 kPa helium canister pressure were analyzed at steady state in Durbin and Lindgren 2017. Other heat loads and canister pressures were analyzed for flow through the cask system, but the duration of the tests is not long enough to reach thermal steady-state conditions. The STAR-CCM+ CFD modeling efforts were focused on those two cases for which steady-state results are available.

An additional CFD model of this same experiment was completed by the NRC and is documented in NRC 2020. A more limited set of results from NRC (2020) is available, so only 5.0 kW at 100 kPa of helium are used to compare against the experiment and STAR-CCM+ models for the crosswind cases.

Overall, the STAR-CCM+ model compared well with the experimental results for the 1.0-kW, 100-kPa cases. The normalized air mass flow rate (mfr/mfr_stagnant) compared very well with a slight difference between the two at 5.3 m/s crosswind velocity. The cladding temperature response was more significant for the STAR-CCM+ model with an increase of maximum cladding temperature of ~4K at 5.3 m/s crosswind velocity over the stagnant case. The experimental temperature only increased ~2K.

For the 5.0 kW, 100 kPa canister helium pressure case, both the CFD model and the experimental results compared well. Both CFD models show an ~10K rise in maximum cladding temperature at 5.3 m/s crosswind over the stagnant case. The experiment showed an ~6K rise in maximum cladding temperature, which is slightly less than results from the CFD models. This is consistent with the previous 1.0 kW, 100 kPa cases. The normalized mass flow rates for the STAR-CCM+ CFD model and the experiment compared very well to each other for the lower wind speeds. For the highest wind speed case (5.3 m/s), there was a slight difference in normalized mass flow between the STAR-CCM+ model and experimental results. The NRC case was just the opposite. There was a slight difference between the experimental results and NRC CFD model for the lower wind speeds, but the result at the highest wind speed was very close.

Table 2.10. STAR-CCM+ Cross Wind Flow Results

Case	Cladding (K)	Delta Cladding (K)	Air Flow (kg/s)	mfr/mfr_stagnant
1.0kW, 100kPa, 0m/s	436	0	3.47E-02	1.00
1.0kW, 100kPa, 1.3m/s	438	2	2.96E-02	0.85
1.0kW, 100kPa, 2.7m/s	440	4	2.30E-02	0.66
1.0kW, 100kPa, 5.3m/s	440	4	2.12E-02	0.61
5.0kW, 100kPa, 0m/s	702	0	6.79E-02	1.00
5.0kW, 100kPa, 1.4m/s	707	5	5.43E-02	0.80
5.0kW, 100kPa, 2.7m/s	711	9	4.37E-02	0.64
5.0kW, 100kPa, 5.3m/s	713	11	3.49E-02	0.51

Table 2.11. Experimental Cross Wind Results (Durbin and Lindgren 2017)

Case	Cladding (K)	Delta Cladding (K)	Air Flow (kg/s)	mfr/mfr_stagnant
1.0kW, 100kPa, 0m/s	433	0	3.61E-02	1.00
1.0kW, 100kPa, 1.4m/s	433	0	2.96E-02	0.72
1.0kW, 100kPa, 2.8m/s	434	1	1.60E-02	0.54
1.0kW, 100kPa, 5.3m/s	435	2	1.02E-02	0.64
5.0kW, 100kPa, 0m/s	704	0	6.99E-02	1.00
5.0kW, 100kPa, 1.4m/s	706	2	5.70E-02	0.82
5.0kW, 100kPa, 2.7m/s	708	4	4.50E-02	0.64
5.0kW, 100kPa, 5.3m/s	710	6	4.20E-02	0.60

Table 2.12. Additional CFD Modeling Results from NRC (2020)

Case	Cladding (K)	Delta Cladding (K)	Air Flow (kg/s)	mfr/mfr_stagnant
5.0kW, 100kPa, 0m/s	713	0	6.74E-02	1.00
5.0kW, 100kPa, 1.34m/s	715	2	6.06E-02	0.90
5.0kW, 100kPa, 2.68m/s	719	6	4.74E-02	0.70
5.0kW, 100kPa, 5.36m/s	723	10	3.25E-02	0.48

Figure 2-17 shows the axial airflow profile of the different crosswind velocities for the 5.0 kW, 100 kPa case. For the most part, airflow enters in one side of the outlet and exits the other. This is the same for the inlet. Effectively, the wind is blowing across the inlet and outlet openings. This flow inhibits air flow down the belowground shell and up around the canister, which leads to lower air mass flow rates through the VDCS and higher maximum cladding temperatures. The CYBL forms a somewhat confined space. Some of the crosswind flow hits the opposite wall of the CYBL and recirculates down, back, and up out of the top. This recirculation is insignificant compared to the initial crosswind flow.

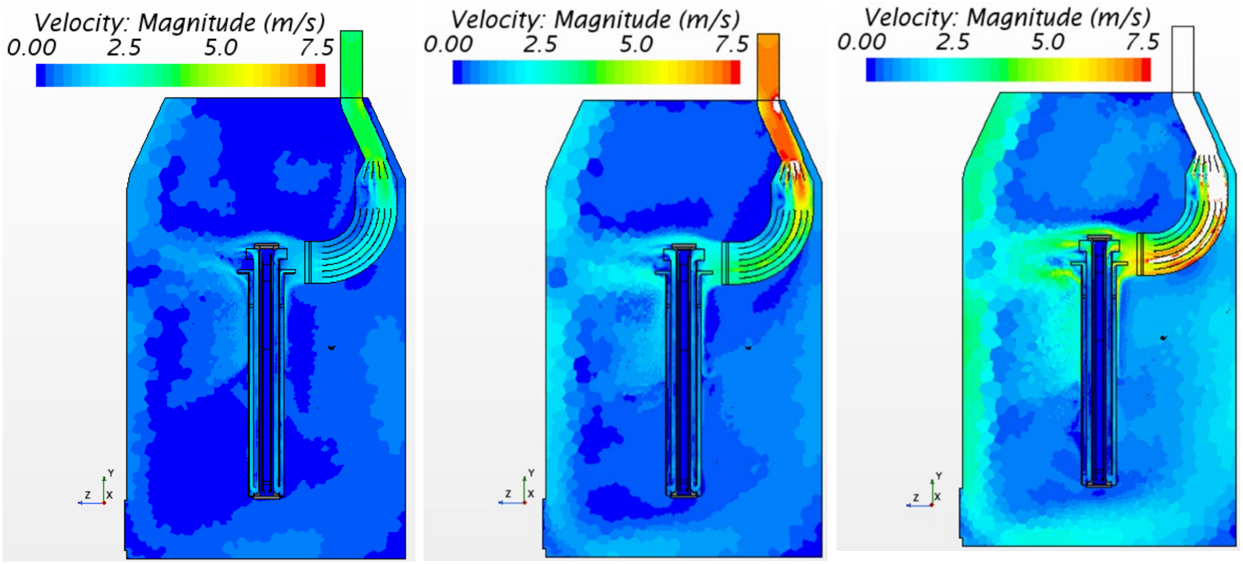

1.4 m/s crosswind 2.7 m/s crosswind 5.3 m/s crosswind

Figure 2-17. Axial Velocity Profile of 5kW, 100kPa Case

Figure 2-18 shows the flow profile in the belowground shell of the VDCS for the STAR-CCM+ CFD model. The experimental flow profile of the belowground shell is included in Figure 2-19 for comparison with the STAR-CCM+ CFD model. The direction of wind flow in both figures is the same. The location of the velocity profile from the STAR-CCM+ model is the same as in the experiment (Durbin and Lindgren 2017). For the stagnant case (0.0 m/s crosswind) the velocity profile in the belowground shell for both the STAR-CCM+ model and experiment compares very well. For the 5.3 m/s case, the STAR-CCM+ profile does not compare as well to the experiment. The two slower speed profiles compare slightly better, but in the STAR-CCM+ profiles, there are regions where high and low velocities are observed. The experimental profiles seem to be much more uniform. More investigation is required to determine the cause for the differences in these flow profiles. Radial belowground shell velocity profiles were not available from NRC (2020).

Figure 2-20 and Figure 2-21 provide further comparisons of the normalized air mass flow rates between the STAR-CCM+ and experimental results for both heat load cases analyzed. Results from NRC (2020) were not available for the 1.0 kW heat load. Overall, everything compared well with each other. Results from the STAR-CCM+ CFD model were very similar to the experimental results for the 1.0 kW case. For the 2.7 m/s crosswind case, there is slight discrepancy which smooths out for the 5.3 m/s crosswind case. For the 5.0 kW case, results from both CFD models were very close to the experimental results with the STAR-CCM+ model diverging slightly for the 5.3 m/s crossflow case. At 5.0 kW heat load for the 2.7 m/s crosswind, the STAR-CCM+ model is very close. The figures provide an additional graphic to visualize the differences between the models and experimental BVDCS.

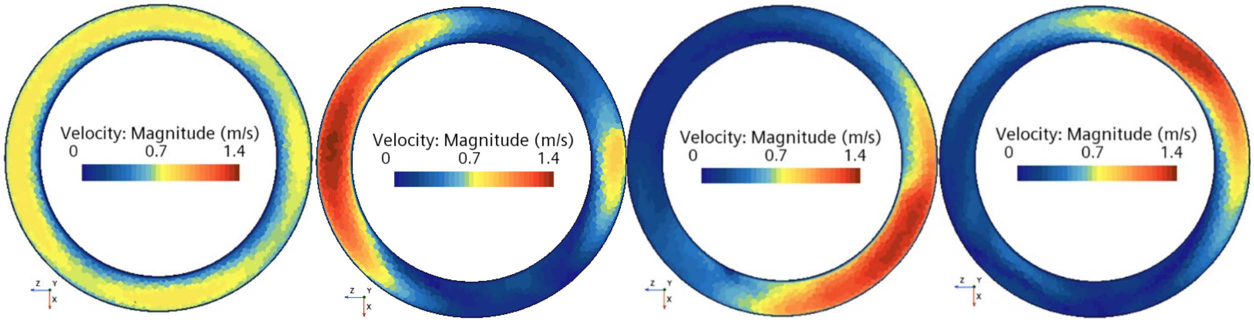

0.0 m/s crosswind 1.3 m/s crosswind 2.7 m/s crosswind 5.3 m/s crosswind

Figure 2-18. STAR-CCM+ Model Belowground Shell Velocity Profile for 5.0 kW, 100 kPa at Various Crosswind Speeds. Wind direction is from right to left matching Figure 2-19.

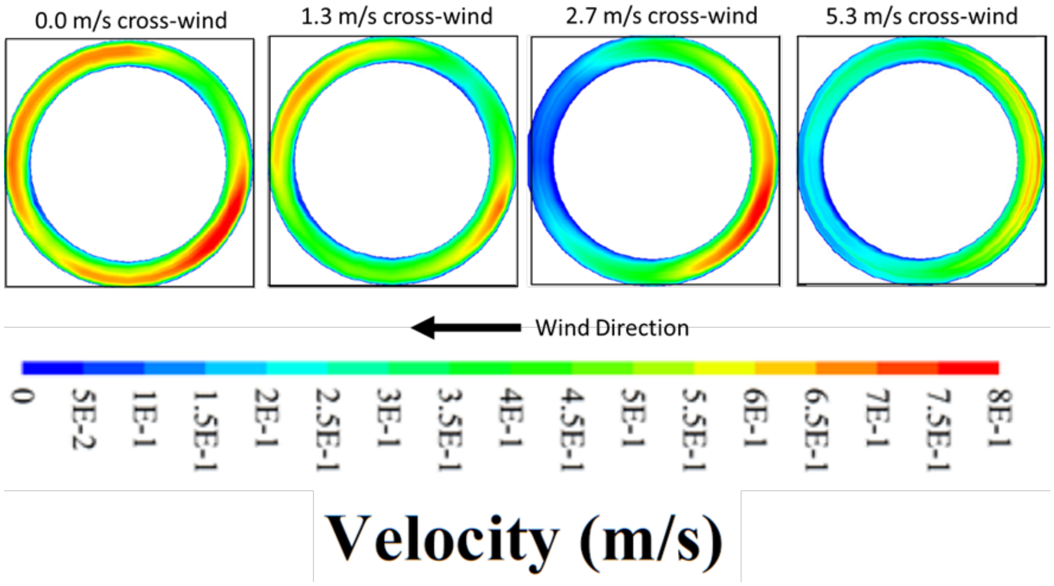

Figure 2-19. Experimental BVDCS Shell Velocity Profiles for 5.0 kW, 100 kPa Case (Figure 4.20 in Durbin and Lindgren 2017)

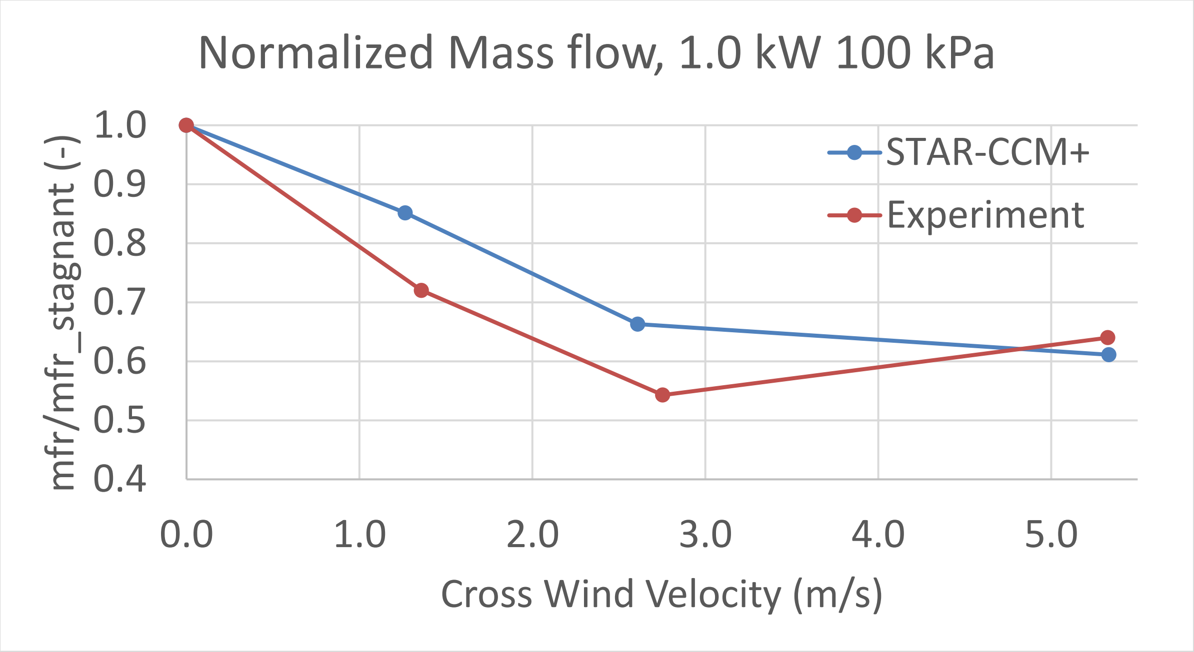

Figure 2-20. Normalized Mass Flow through the VDCS Comparison with the Experiment Conducted in Durbin and Lindgren 2017

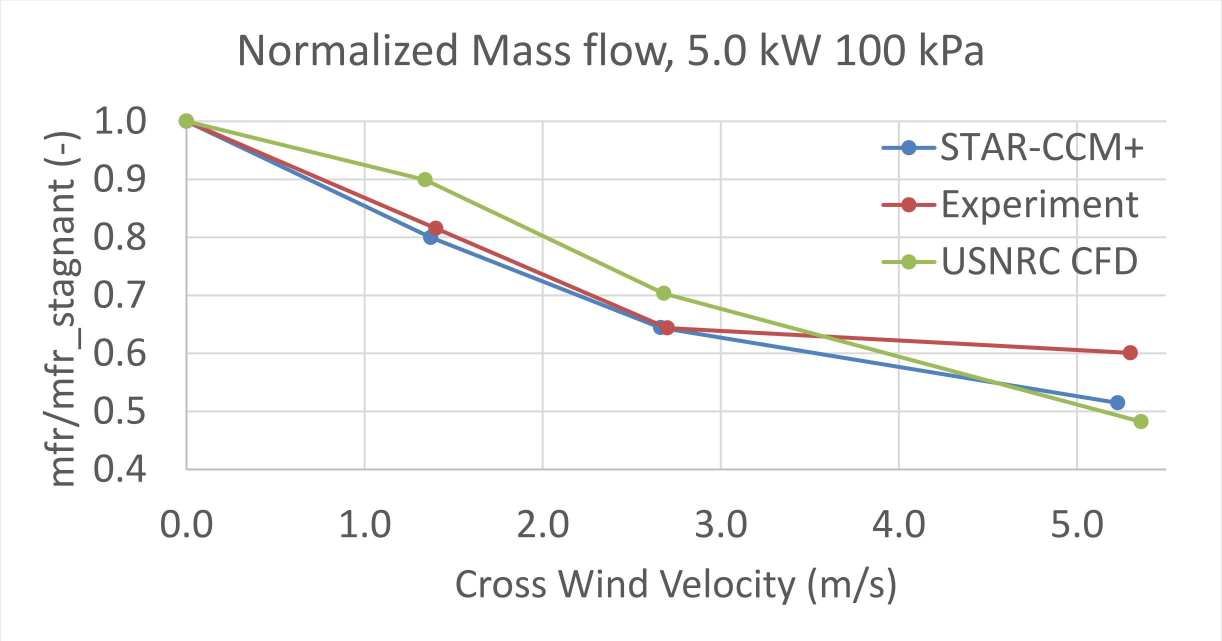

Figure 2-21. Steady-State Normalized Mass Flow Rate Comparison between the STAR-CCM+ Model (this study), Experiment (Durbin and Lindgren 2017), and Additional CFD model (NRC 2020)

2.4 Belowground VDCS Concluding Remarks

The main conclusion from this study is that results from the STAR-CCM+ CFD model of the BVDCS in crossflow compares very well with the experimental results documented by Durbin and Lindgren (2017). The purpose of this study is to perform an initial investigation into the validation of this STAR-CCM+ model. Full models including the external fluid, such as in this study with the CYBL, are much less common than standalone models without a modeled external environment. This study provides support for future research with models that include external environments around these cask systems. Further investigation could be performed to better understand the differences between the STAR-CCM+ models and the experimental model. In addition, improvements could be made to the CFD model in accordance with the sensitivity analysis performed. The STAR-CCM+ model of this BVDCS system compared very well to the experimental BVDCS documented by Durbin and Lindgren (2017) and the NRC CFD model (NRC 2020), which provides support for using these external environment STAR-CCM+ models in the context of SNF dry storage systems.

This page is intentionally left blank

3. SOLAR MODELING

In previous PNNL wind effects models solar loads were neglected. In the standalone models solar loads are modeled with STAR-CCM+'s solar sub-model and an environmental boundary condition. The environmental boundary condition accounts for external radiation and convection heat transfer at an external surface with an external ambient temperature, without explicitly modeling the external environment. Incorporating an explicitly modeled external environment into the wind effects models requires a different method of incorporating solar effects. Because this is a somewhat new method of implementing solar effects in these STAR-CCM+ models, some testing exercises are required. The first exercise compared solar loadings on cask system models with and without the wind effects boundary included in STAR-CCM+. In addition, an identical simplified ANSYS Mechanical ANSYS Parametric Design Language (APDL) model was compared to an identical STAR-CCM+ model. This comparison between APDL and STAR-CCM+ were standalone (i.e., with no wind effects) models. These comparison cases were performed with a single-module NUHOMS® AHSM-HS SNF dry storage cask system used previously by Suffield et al. (2021). These validation cases provide support that the wind effects and non-wind effects implementation of the solar loading models are similar with negligible differences.

3.1 STAR-CCM+ Standalone Comparison to Wind Effects

To ensure that the method of including solar radiation into the wind effects model is well understood a comparison of the wind effects model to the standalone STAR-CCM+ model was conducted. The process for this comparison is to apply the respective solar radiation models and then compare the external surface temperature profiles and maximum external surface temperatures. Solar radiation has been modeled extensively in the past. The purpose of this exercise is to ensure that the solar radiation model in the wind effects matches the better understood solar radiation modeling in the past standalone models.

The NUHOMS® AHSM-HS with a 32PTH2 canister model described in Suffield et al. (2021) was used to compare the solar loading implementation between the standalone and wind effects models. The solar loads are based on insolation data presented in Title 10 of the Code of Federal Regulations, Part 71, "Packaging and Transportation of Radioactive Material" (10 CFR 71) for total heat load over 12 hours. The solar insolation was applied as a solar flux averaged over 24 hours for a steady-state analysis. The following insolation values were applied in the STAR-CCM+ model:

- Flat horizontal surfaces = 775.32 W/m^2
- Curved surfaces = 387.67 W/m^2
- Flat non-horizontal surfaces = 193.83 W/m^2

3.1.1 Standalone Solar Radiation Model Description

In STAR-CCM+, for standalone models with the external environment not explicitly modeled (non-wind effects models), solar radiation is applied with the solar loads model. The STAR-CCM+ solar load model simulates both direct and diffuse radiation loads from the sun. The specified solar radiation is then applied to the boundaries where the external environment condition is specified. For the AHSM-HS the environmental condition is applied to the exterior surfaces of the cask that would interface with the external environment.

3.1.2 Wind Effects Solar Radiation Model Description

For the wind effects model with the external environment explicitly modeled, the environment boundary condition is not available for the outer surfaces of the SNF storage module. To account for solar radiation in the wind effects model, directional radiation flux is applied to the exterior surface of the external environment. The diffuse component is applied to all surfaces that interface with the external environment. For the directional flux a direction is specified, which in this case is configured to model the sun directly overhead of the cask. The directional flux is applied to all surfaces incident to the direction specified. Solar radiation in the wind effects model is modeled much like the sun with the directional radiation being specified at the exterior boundary and being allowed to radiate downwards.

3.1.3 Results of STAR-CCM+ Solar Methods Comparison

To evaluate only the differing implementations in solar radiation, a no heat load condition was applied to the fuel assemblies within the 32PTH2 model. This allowed natural convective flow within the AHSM-HS to be driven only by solar loadings. Table 3.1 shows the resulting temperature comparisons for various components of the system and outside surfaces of the concrete. The average concrete surface temperatures are all within 3°C of one another except for the horizontal surfaces and sides of the door. The side of the door is ~6°C warmer for the wind effects model than the standalone model. One possible explanation for this can be deduced from the outside temperature profiles of the concrete for the standalone and wind effects models shown in Figure 3-1. When comparing these profiles, it is evident in the wind effects model that there are higher temperatures on the sides of the door and around the bottom of the cask overpack. It appears that these higher temperatures could be caused from solar radiation reflecting from the ground surrounding cask system. This ground is absent in the standalone model. The differing temperature profiles on the cask door will likely have a negligible effect on the PCT and canister temperatures inside of the cask system.

Overall, both models compare very well. This indicates that both methods of implementing solar radiation yield similar results, and implementation of solar radiation in the wind effects models is consistent with previous standalone models that have been used extensively. This provides further support and understanding for using the wind effects model of these dry storage cask systems.

Table 3.1. Surface Temperature Results for Standalone and Wind Effects AHSM-HS Models

Model	Heat Load (kW)	Avg Canister Temp. (°C)	Max Canister Temp. (°C)	Concrete Temps (°C)					
				Back	Front	Side	Top	Door Front	Door Side
Standalone	0	40	41	45	46	46	60	45	47
Wind Effects	0	42	43	47	48	47	59	48	53

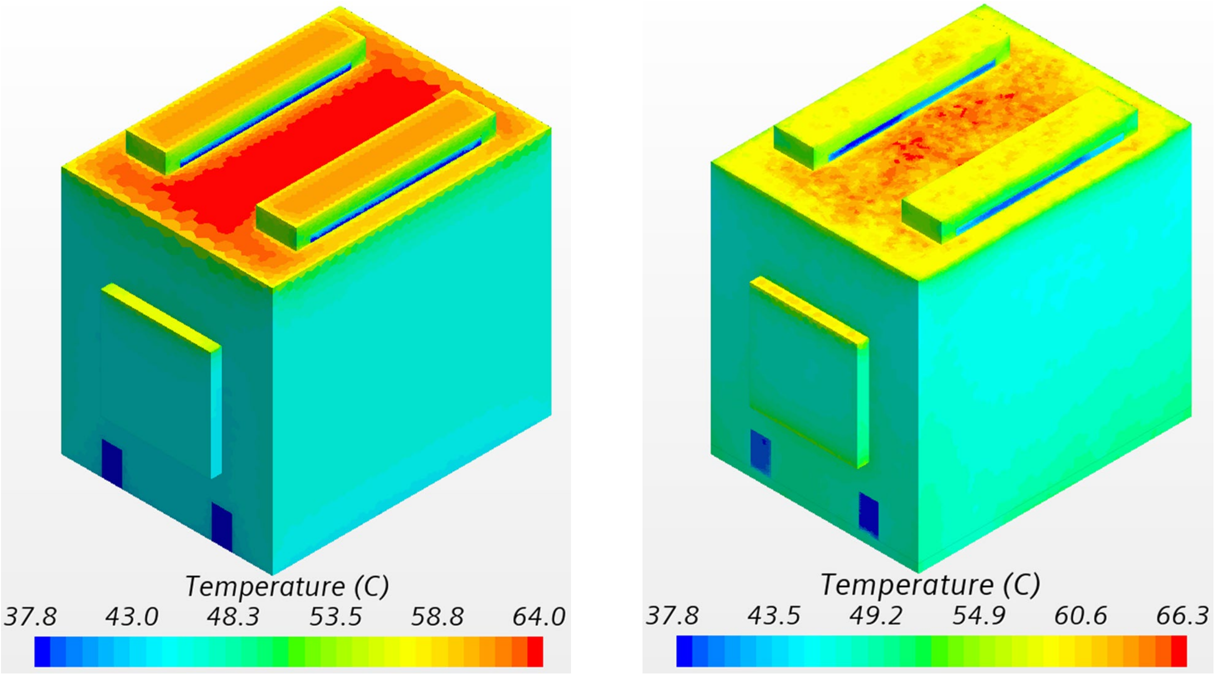

(a) standalone model (b) wind effects model

Figure 3-1. External Concrete Temperature of AHSM-HS with Solar Loadings Applied

3.2 STAR-CCM+ and ANSYS Mechanical APDL Solar Model Comparison

For the model comparison between STAR-CCM+ and APDL, the same storage module configuration used for the previous STAR-CCM+ model comparison was used except all of the internal components were removed. Only the concrete overpack, door, and air inside of the cask were modeled. Convection and any heat load inside the cask were ignored. Solar radiation is the only thermal source in these models. For this comparison, the standalone solar models are compared. The wind effects boundary is left out of these simplified models. This provides a very computationally efficient model with differences limited only to variations in the amount of solar insolation. This approach provides a direct comparison of the implementation of the solar model in STAR-CCM+ to APDL. Both models followed 12 hour averaged heat loads specified in 10 CFR 71 and described earlier for the previous STAR-CCM+ model comparison.

3.2.1 STAR-CCM+ Solar Model

For this comparison, a standalone STAR-CCM+ solar model was used. The solar model involves setting the directional and diffuse radiation fluxes through the physics models. Then, an environmental thermal boundary condition on the desired surfaces is set to apply the solar radiation automatically. Along with the solar radiation being defined on the environmental boundary, a heat transfer coefficient of 5.0 W/m^2-K is applied. This heat transfer coefficient is meant to roughly represent free convection and conduction from the concrete to the external environment. This same heat transfer coefficient is applied in the APDL model to isolate differences to the solar models. In the STAR-CCM+ model, the solar radiation is applied as a combination of directional and diffuse flux. The directional flux is configured to model the sun directly overhead. The majority of the radiation flux is applied via directional flux. The remaining flux is applied as diffuse. Application of the solar radiation was described previously in Section 3.1.

3.2.2 APDL Model

APDL is a coding language that uses the ANSYS finite element solver to simulate a multitude of mechanical systems (ANSYS 2016). For our purposes, the thermal finite element capabilities of the code allow direct imposition of solar heat flux boundary conditions onto the exterior surfaces of the model geometry. This differs from the approach used when developing models using STAR-CCM in which the insolation cannot be defined explicitly. APDL was used as a confirmatory tool to verify that the thermal response due to insolation of the STAR-CCM+ model was realistic.

A simplified APDL model of a single NUHOMS® module was developed for this study. The model parameters include the external natural convection coefficients, external radiation exchange factors, and the heat flux incident on the external surfaces due to insolation. The heat flux incident on the external surface was set in accordance with 10 CFR 71 and the other parameters were set based on past modeling experience. In an effort to isolate the effect of insolation, heat transfer due to internal natural convection and internal radiation is ignored in this model. For all external surfaces, the natural convection coefficient was set to a value of 5.0 W/m^2-K, which is representative of most SNF storage systems.

APDL provides a straightforward approach for applying heat flux boundary conditions in comparison to STAR-CCM+. Using surface elements overlaid onto the external surfaces of the model geometry, a heat flux can be defined per unit surface area and provides a direct approach for defining the insolation heat flux. This comparison with STAR-CCM+ will verify that the implementation of solar radiation in STAR-CCM+ is behaving as expected.

3.2.3 Solar Loading Results Comparison

Table 3.2 and Table 3.3 show the temperatures for selected surfaces for the STAR-CCM+ and APDL models, respectively. Figure 3-2 and Figure 3-3 show the temperature profiles of the exterior of the cask system for the STAR-CCM+ and APDL models, respectively. The maximum temperatures between the STAR-CCM+ model in Table 3.2 and the APDL model in Table 3.3 are close to each other except for the door surface. The APDL temperatures on the door surface are significantly higher than temperatures on the other surfaces, which indicates that this could be due to some factor other than the implementation of the solar model. The main take away is that the STAR-CCM+ models matched the ANSY APDL models very well. This builds confidence in these solar insolation models used in STAR-CCM+ for both standalone and wind effects models.

Table 3.2. STAR-CCM+ Model Temperatures of Selected Surfaces with 12-Hour Averaged Solar Insolation

Surface	Max Temp. (K)	Min Temp. (K)	Avg Temp. (K)
Overpack Top	367	343	361
Overpack Sides	347	325	328
Vent Top	363	345	359
Vent Sides	352	335	328
Door Surface	351	342	349

Table 3.3. APDL Model Temperatures of Selected Surfaces with 12-Hour Averaged Solar Insolation

Surface	Max Temp. (K)	Min Temp. (K)	Avg Temp. (K)
Overpack Top	370	345	364
Overpack Sides	358	328	329
Vent Top	359	344	356
Vent Sides	362	331	339
Door Surface	401	340	376

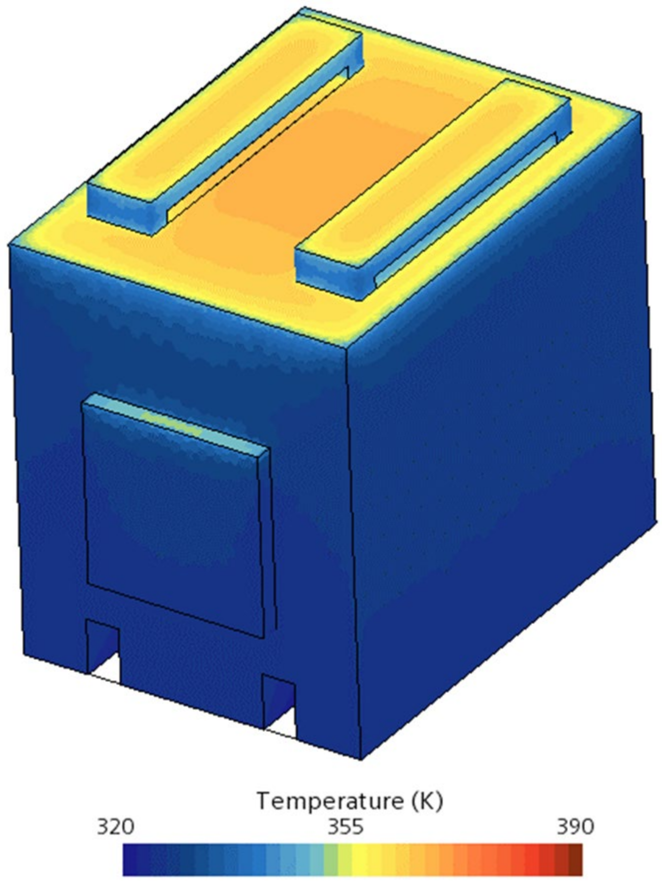

Figure 3-2. STAR CCM+ Model External Concrete Thermal Profile

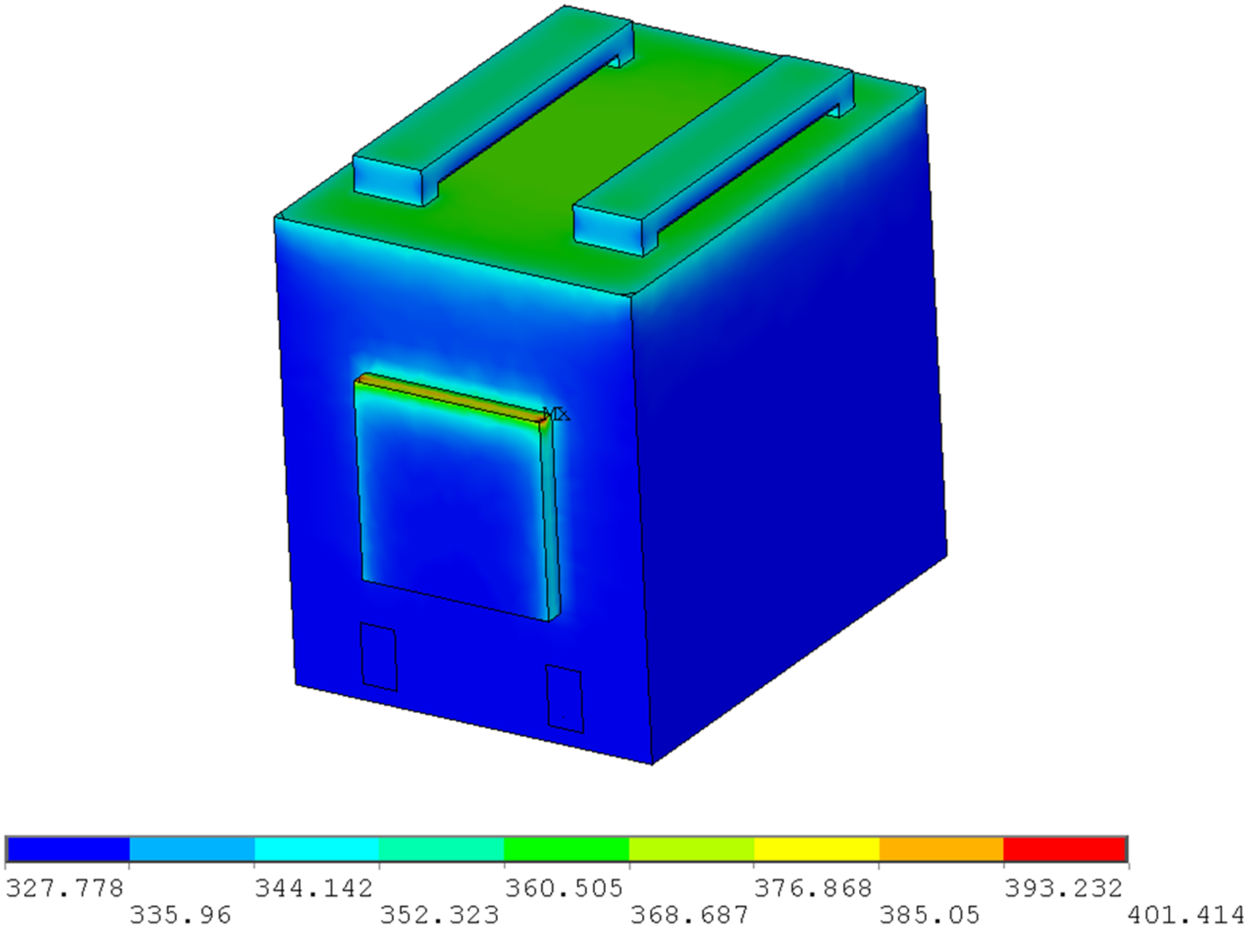

Figure 3-3. APDL Model External Concrete Temperature Profile [K]

4. NUHOMS® MODELS

Variations of the NUHOMS® dry storage system were modeled; a site-specific horizontal storage module (HSM) and the AHSM-HS. The site-specific configuration is used at the Calvert Cliffs nuclear power station; thermal models for two of the loaded modules at that site, HSM-1 and HSM-15, are described in detail in Suffield et al. 2012. The HSM-15 thermal model was adapted for wind effects as described in Jensen et. al 2020. The AHSM-HS model is described in detail in Suffield et. al. (2021). Sensitivity analyses were run with each model to look at the thermal and flow response of the model to changing wind direction and speed. The HSM-15 is a convenient model for initial investigation while the AHSM-HS model was being developed. Further investigation following this study will be done with the AHSM-HS in support of the CDFD. A description of the sensitivity analyses and results are given in this section.

4.1 HSM-15 Model

4.1.1 Model Description

In the previous fiscal year 2020 report (Jensen et al. 2020), extensive external fluid modeling for the HSM-15 was conducted for particle deposition analysis. As part of this analysis, wind directions in 30° increments at four different wind speeds were analyzed. The cases where the wind direction is 90° to the cask is of particular interest to this wind effects report because it has similar characteristics to the confirmatory modeling described in Section 2. When the wind direction is oriented at 90° to the HSM, the flow is parallel to the inlets and the outlets much like that described for the BVDCS in Section 2.

The details of this model and how it was constructed can be found in Jensen et al. (2020). The exterior geometry of this model is shown in Figure 4-1. The model with the external fluid region fitted is shown in Figure 4-2. The model is developed as an initial look at external wind effects and particle deposition, so there is more work to be done to further refine, verify, and validate the model. For this model, the cask and canister have been simplified by removing the detailed interior of the dry storage canister including the porous fuel assemblies. The heat source has been replaced by an equivalent heat flux profile from a standalone model of this same HSM-15 applied to the inner surface of the Dry Storage Canister (DSC). This method works well for developing a computationally efficient model with the addition of an external environment. Along with including the details of the interior of the canister, further developments to the external wind boundary will be made.

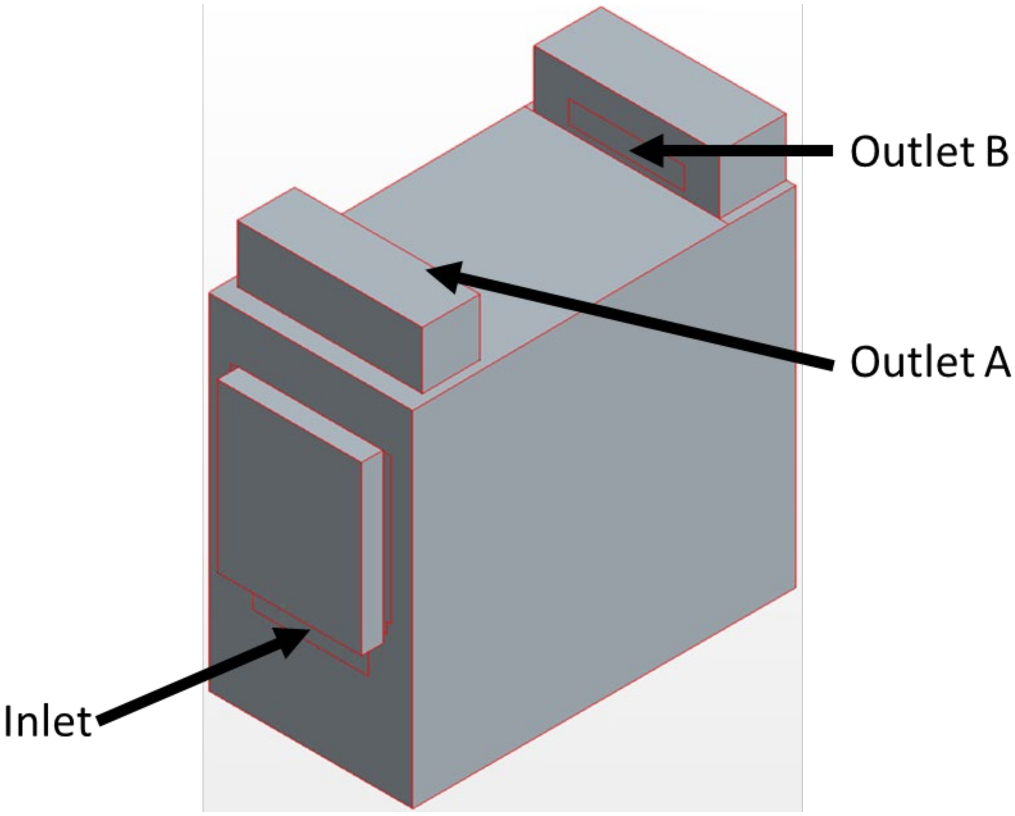

Figure 4-1. HSM-15 from Jensen et al. 2020 used for the Directional and Winds Speed External Environment Tests

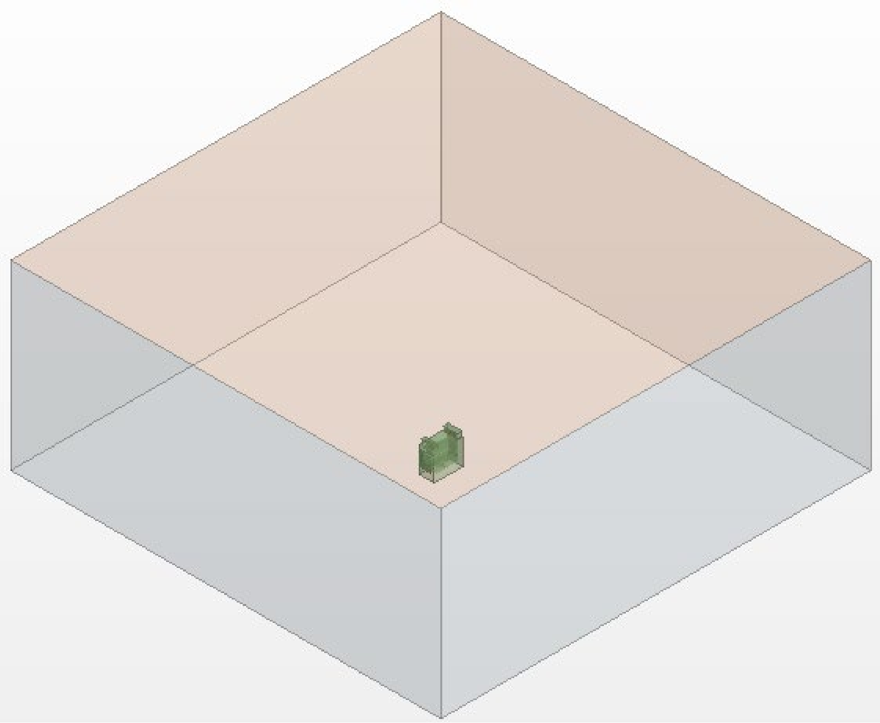

Figure 4-2. NUHOMS® HSM-15 with external fluid boundary

4.1.2 Thermal and Flow Response

For this report, the thermal and flow results from the HSM-15 with cross wind conditions matching the BVDCS were of particular importance. Table 4.1 through Table 4.4 shows thermal and flow responses to increasing wind speeds for two different wind directions—90° and 0°. The 0° and 90° cases show the differences that wind direction has on flow and thermal responses.

Table 4.1 shows the impact of increasing wind speed on the maximum DSC temperature and mass flow through the cask with a heat load of 35 kW. For the lower wind speeds at 2.5 m/s, 5.0 m/s, and 15.0 m/s, the thermal and flow responses match the trends in the BVDCS modeling shown previously in Table 2.10 with increasing DSC temperatures and decreasing flow through the cask for increased crosswind speeds for this 35 kW heat load case. But unlike the BVDCS case, the 2.5 m/s wind speed results in a lower temperature than the stagnant 0.0 m/s wind case. This is possibly due to geometry differences and implementation of the crosswind. In the BVDCS modeling, the wind machine only directs air over the outlets and inlets; whereas, in the HSM-15 model, wind is directed over the entire cask system. Also, in real life, these cask systems are joined side to side with each other so it is possible that in the more realistic configuration these HSM-15 cask systems could behave much closer to the BVDCS in a crosswind. This is a point for future research. For the 26.5 m/s crosswind at 90°, the temperature decreases significantly from the 15.0 m/s cases and has the lowest average and maximum DSC temperatures. It appears that there is significant back flow from one of the outlets through the inlet. This seems to be a significant difference from the lower wind speed cases. Determining the conditions in which the flow regime transitions to backflow is another area for further research.

Table 4.1. 35-kW 90° Wind Thermal and Mass Flow Response (Into (+) and Out of (-) the Cask) with Increasing Wind Speeds

Wind Speed [m/s]	Max. DSC Temp. (°C)	Avg. DSC Temp. (°C)	Mass Flow Inlet (kg/s)	Mass Flow Outlet A (kg/s)	Mass Flow Outlet B (kg/s)	mfr_inlet/ mfr_stagnant
0.0	313	156	5.85E-01	-2.62E-01	-3.25E-01	1.00
2.5	313	153	5.71E-01	-2.53E-01	-3.17E-01	0.98
5.0	312	154	5.07E-01	-2.21E-01	-2.81E-01	0.87
15.0	310	162	2.38E-02	3.97E-01	-3.86E-01	0.04
26.5	293	151	-7.63E-01	7.15E-01	-2.05E-02	-1.30

In addition to the 35-kW heat load cases, the 5-kW heat load case at different wind speeds at 90° also are presented in Table 4.2. For the lower wind speed cases the thermal and flow responses are similar to the 35-kW case. The average temperature of the canister is higher for the stagnant case than the 2.5 m/s cross wind cases. The canister temperatures increase from the 2.5 m/s crosswind to 5.0 m/s. One major difference from the 35-kW, is in the 5-kW cases backflow exists sooner at 15.0 m/s rather than at 26.5 m/s for the 35-kW case. Strength of natural convection inside of the cask due to heat in the canister is a possible factor contributing to the backflow at lower crosswind speeds for the 5 kW heat load cases. For future investigation, an empty cask could contribute to supporting or disproving this hypothesis.

Table 4.2. 5-kW 90° Wind Thermal and Mass Flow Response (Into (+) and Out of (-) the Cask) with Increasing Wind Speeds

Wind Speed (m/s)	Max DSC Temp (°C)	Avg. DSC Temp (°C)	Mass Flow Inlet (kg/s)	Mass Flow Outlet A (kg/s)	Mass Flow Outlet B (kg/s)	mfr_inlet/ mfr_stagnant
0.0	104	56	3.03E-01	-1.40E-01	-1.62E-01	1.00
2.5	100	52	3.29E-01	-1.44E-01	-1.68E-01	1.08
5.0	103	56	1.55E-01	6.68E-02	-2.18E-01	0.51
15.0	84	50	-3.33E-01	4.41E-01	-8.83E-02	-1.10
26.5	70	44	-7.00E-01	6.98E-01	-5.14E-02	-2.31

Figure 4-3 and Figure 4-4 further visualize the flow responses of the canister for the 90° wind case. Figure 4-3 shows a plot of the normalized inlet mass flow as a function of wind speed. The trend is initially decreasing flow through the inlet as wind speed increases. Then the flow transitions to significant backflow. At 26.5 m/s cross wind speed both 35 kW and 5 kW cases experience backflow greater than the initial stagnant flow. One interesting point is at 15 m/s cross wind the inlet mass flow is nearly zero for the 35 kW case where the 5 kW case experiences backflow nearly equal to the magnitude of flow in the stagnant case.

Figure 4-4 shows a vector plot of a cross section of the cask at the middle of the cask inlet. This section is shown as looking down on the top of the cask. The two vector plots are for the 35 kW case at 26.5 m/s (Figure 4-4a) and 5.0 m/s (Figure 4-4b) crosswind both at 90° to the cask. These wind speeds were chosen because of the very different flow profiles at the inlet for these two cases. The 5 m/s case has inflow where the 26.5 m/s case has primarily outflow. At this cross section, Figure 4-4(a) shows a significant recirculation at the inlet plane. Whereas, in Figure 4-4(b) the flow is primarily into the cask system. It appears that the flow is straighter into the cask on the downwind side and more parallel to the inlet on the up-wind side. Comparing the two plots, the swirl and turbulence in the eddy in front of the inlet have a significant impact on the flow profile of the inlet. From looking at the mass flow rates and flow profiles for the 35-kW case, it appears there is a transition of the flow on the inlet from 15.0 m/s to 26.5 m/s where the magnitude of mass flow on the inlet reverses. A similar transition takes places for the 5-kW case from 5.0 m/s to 15 m/s crosswind velocity.

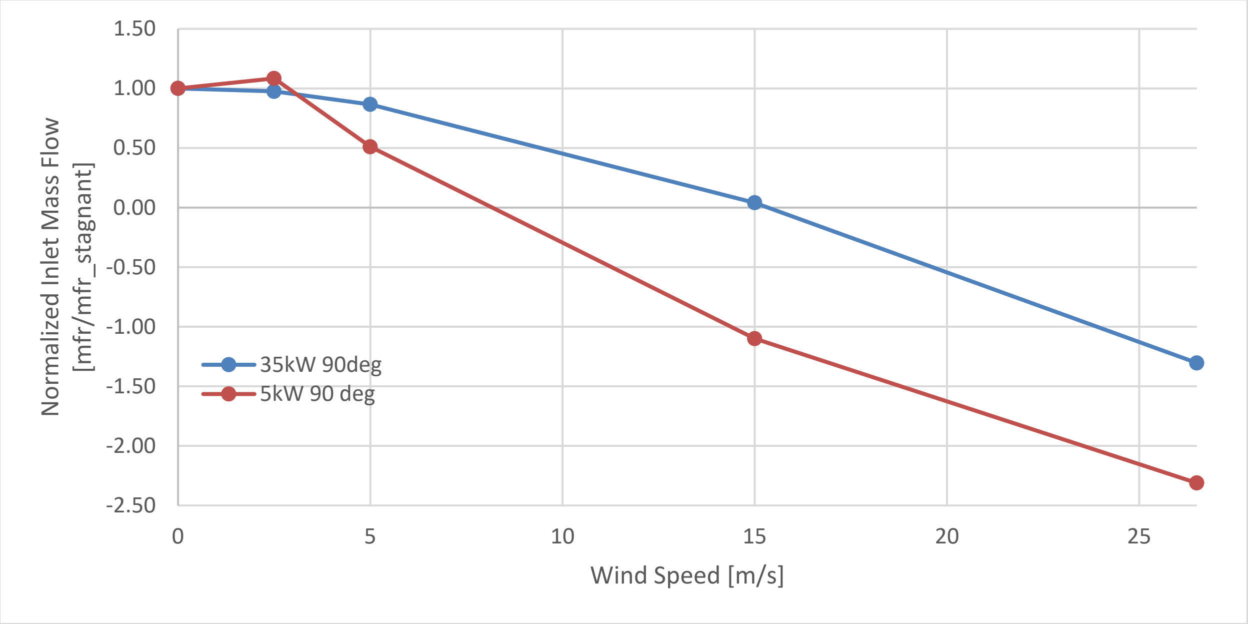

Figure 4-3. Normalized Mass Flowrates for the 90° Wind Direction Cases

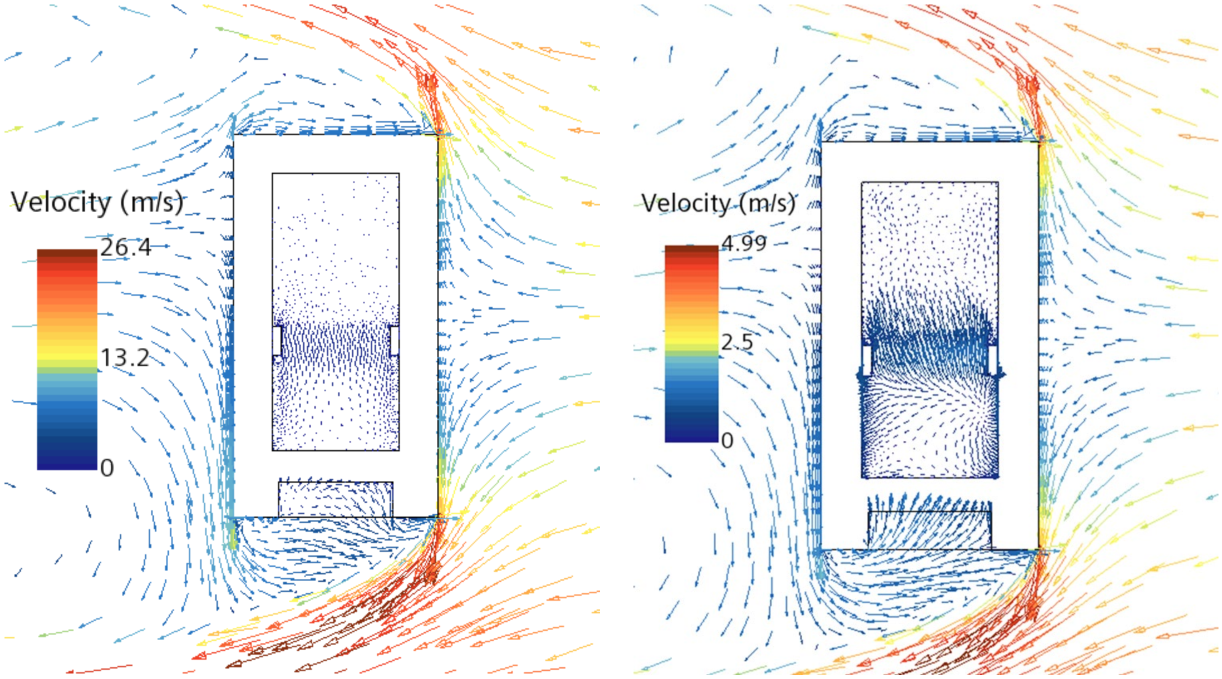

(a) 26.5 m/s

(b) 5.0 m/s

Figure 4-4. Cross Section at Inlet Flow Comparison at Two Different Wind Speeds at 90° for the 35-kW Heat Load Case

In addition to the 90° cases, the same runs with increasing wind velocities were completed with a 0° head on wind direction. The results from these runs are shown in Table 4.3 and Table 4.4 for the 35 kW and 5 kW heat load cases, respectively. Compared to the previous 90° cases, the results from the 0° cases are as would be expected. As the wind speed increases, more air is forced through the cask system, which results in drastically improved cooling with lower canister temperatures. At the highest wind speed for the 35-kW case, the wind-induced air flow is 12.6 times higher than the stagnant case. For wind speeds from 5.0 m/s to 26.5 m/s, both the 35 kW and 5 kW heat load cases have similar magnitudes of flow rates through the cask and the normalized flowrates for the 5 kW case being about twice the normalized flowrates for the 35 kW case. This possibly indicates that at 0° wind directions above 5.0 m/s, flow through the cask has been dominated by the wind. A topic for future investigation is to further explore the relationship between forced (wind-driven) and natural convection through these cask systems. One future objective is to determine the specific conditions in which wind-driven flows dominate natural convection caused by the heat load inside of the cask.

Table 4.3. 35-kW, 0° Wind Thermal and Mass Flow Response (Into (+) and Out of (-) the Cask) with Increasing Wind Speeds

Wind Speed [m/s]	Max DSC Temp (°C)	Avg. DSC Temp (°C)	Mass Flow Inlet (kg/s)	Mass Flow Outlet A (kg/s)	Mass Flow Outlet B (kg/s)	mfr_inlet/mfr_stagnant
0.0	313	156	5.85E-01	-2.62E-01	-3.25E-01	1.00
2.5	304	148	8.75E-01	-3.63E-01	-5.13E-01	1.49
5.0	302	143	1.42E+00	-6.67E-01	-7.60E-01	2.42
15.0	252	109	4.22E+00	-1.73E+00	-2.50E+00	7.21
26.5	231	92	7.36E+00	-2.96E+00	-4.42E+00	12.58

Table 4.4. 5-kW, 0° Wind Thermal and Mass Flow Response (Into (+) and Out of (-) the Cask) with Increasing Wind Speeds

Wind Speed [m/s]	Max DSC Temp (°C)	Avg. DSC Temp (°C)	Mass Flow Inlet (kg/s)	Mass Flow Outlet A (kg/s)	Mass Flow Outlet B (kg/s)]	mfr_inlet/mfr_stagnant
0.0	104	56	3.03E-01	-1.40E-01	-1.62E-01	1.00
2.5	97	48	7.37E-01	-3.19E-01	-4.09E-01	2.43
5.0	88	47	1.39E+00	-5.71E-01	-8.17E-01	4.58
15.0	64	34	4.26E+00	-1.74E+00	-2.52E+00	14.07
26.5	53	30	7.54E+00	-3.09E+00	-4.45E+00	24.87

4.2 AHSM-HS Model

In addition to the site specific HSM-15, a single standalone AHSM-HS thermal model described in Suffield et al. (2021) is used for investigating wind effects modeling. The primary use of this model is to support the CDFD effort. The work presented in the previous sections was applied to the development of wind effects models of the AHSM-HS and guide further investigations with the AHSM-HS model. The following sections provide a description of the current progress on developing an AHSM-HS wind effects model to provide a better understanding of future modeling efforts and improvements to this model.

4.2.1 Model Setup

For this modeling effort an AHSM-HS standalone model and wind effects model developed previously in Suffield et al. 2021 is used. Both standalone and wind effects models are configured with a 40kW heat load, 38°C (100°F) ambient temperature, and identical cask internals. The only difference between the two models is how the external environment is modeled. In the standalone model, the external environment is modeled with an environmental boundary condition. The environmental boundary condition accounts for external radiation and convection heat transfer at a surface with an external ambient temperature. The external convection is calculated using natural convection correlations for different surface geometries. In the wind effects model, the external environment is modeled explicitly using an external region for the external flow.

This wind effects model is set up with a 55-meter radius semi sphere to model external fluid (wind) flowing over the cask shown in Figure 4-5. This was loosely based on best practices for vehicle external aerodynamics on an open road (Siemens 2020a). The flow domain comes out to about 9 times the length of the casks analyzed. Using a halfsphere rather than a square box domain in the previous HSM-15 model allows for rotating the flow around the cask without having to change the boundary types on the desired inflow and outflow boundaries. The semi sphere boundary is recommended for external aerodynamics involving aerospace vehicles (Siemens 2020b). The wind flow for this study is incompressible at less than Mach 0.3, which allows for use of a smaller boundary region. This semi sphere boundary enables these cask system models to be used for a variety of studies, which is helpful for wind effects and particle deposition studies. This single AHSM-HS wind effects model was used to run sensitivities to wind direction. Adding this semi-spherical boundary is an improved design update made after the initial HSM-15 wind effects model.

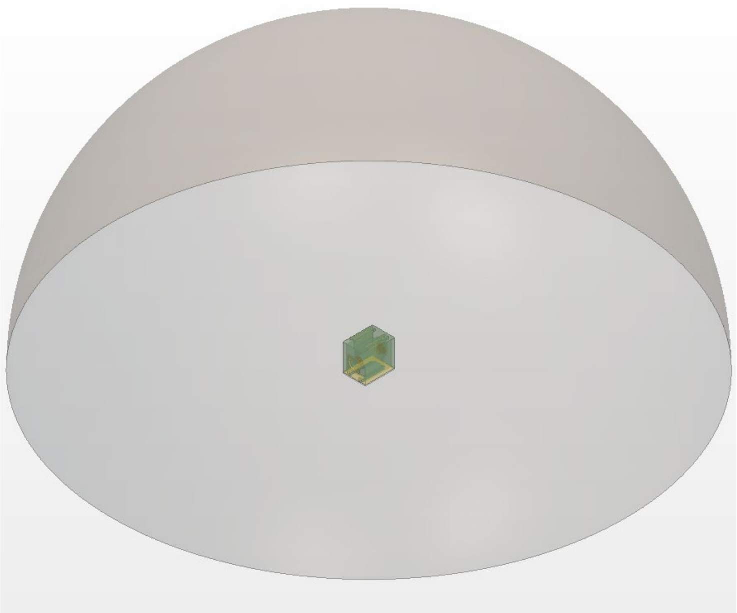

Figure 4-5. Single AHSM-HS with External Fluid Boundary Applied

The NUHOMS® HSM-15 in Section 4.1 found backflow through one of the outlets at certain wind directions. For this current study a wind sweep was performed on a single module AHSM-HS wind effects model to determine the flow and thermal response and determine if backflow conditions exist. The thermal and flow response will also be compared to the previous BVDCS and HSM-15 models to determine consistencies between these models. This wind sweep was performed by changing the wind direction in 30° increments with 0° being normal to the inlets of the cask. The 45° and 135° wind directions were also tested. All wind directions were run with a 5 m/s wind speed. These test conditions are similar to the previous wind effects study on the HSM-15 model.

4.2.2 AHSM-HS Thermal and Flow Response

To form a baseline case and compare the standalone to the wind effects models, both models were initially run under stagnant, no wind, conditions. These results are presented for the temperature comparison in Table 4.5, and flow comparison in Table 4.6. The difference in temperature between these two models is 1°C for the PCT, which is very close. This provides verification that these models are both very similar despite the difference in how the external environment is modeled. The canister and average cladding temperature compared very well also. The inlet mass flow rates for the two models were almost identical with a difference of less than 0.01 kg/s. The inlets and outlets specified in Table 4.6 are shown in Figure 4-6.

The results from the wind direction sweep using the wind effects AHSM-HS model are shown in Table 4.7 for the thermal response and Table 4.8 for the flow response. Looking at Table 4.7, as the wind direction moved from the normal, 0° to 90° cross wind, the cladding and canister temperatures increased. At 90° the maximum and average cladding temperatures were higher than the same wind effects model under stagnant conditions shown in Table 4.5. When looking at the Table 4.8, the mass flow rate for a 90° wind direction is lower than in the stagnant case, which contributes to the increased temperatures of the cladding and canister. This is a similar trend that has been seen previously with the HSM-15 and BVDCS. Further investigation is required to determine if this trend matches the previous examples for different wind speeds with the AHSM-HS. Running different wind speeds to further understand the effect of wind on the flow and temperature of the cask is a topic of future research. From the 90° direction to the 180° direction, with the wind at the back of the cask, the temperature decreases and the mass flow increases. For the 180° case the temperatures are lower than the stagnant case but still warmer than the 0° wind direction case.

The full wind sweep mass flow rates for the single AHSM-HS are shown in Table 4.8. Positive mass flow is into the cask and negative is out. For all wind directions there is little evidence of backflow through the outlets of the cask as all mass flow rates are negative. For the 135° wind direction, back quartering direction, the mass flow through the left outlet was relatively low, which indicates a higher likelihood of backflow occurring through that outlet, but the mass flow out of that outlet is still negative, which indicates outflow. The locations of the inlets and outlets are depicted in Figure 4-6. For a 5 m/s wind speed at 135° there is no backflow, but further investigation is necessary to determine that this holds for all windspeeds. The AHSM-HS outlets are open on two sides, allowing wind-blown air to pass from one side of the outlet to the other, instead of taking a 90° turn into the AHSM-HS module. The outlet geometry for the HSM-15 is different and is likely more conducive to backflow. Outlet geometry is an important factor in the development of backflow. It is also important to note that it has not been determined if backflow has any adverse impacts. Some designs may be more susceptible to backflow than others and further investigation of backflow conditions and its impact is recommended.

Table 4.5. AHSM-HS temperature comparison between standalone and wind effects models under stagnant conditions

Model	Max Temp Cladding [°C]	Max Temp Canister [°C]	Average Temp. Cladding [°C]	Average Temp. Canister [°C]
Stand Alone Single Module	407	218	288	180
Wind Effects Single Module	406	216	288	179

Table 4.6. AHSM-HS mass flow rate comparison between standalone and wind effects models under stagnant conditions

Model	Mass Flow Inlet Left [kg/s]	Mass Flow Inlet Right [kg/s]	Mass Flow Outlet Left [kg/s]	Mass Flow Outlet Right [kg/s]
Stand Alone Single Module	0.37	0.37	-0.369	-0.379
Wind Effects Single Module	0.37	0.36	-0.38	-0.35

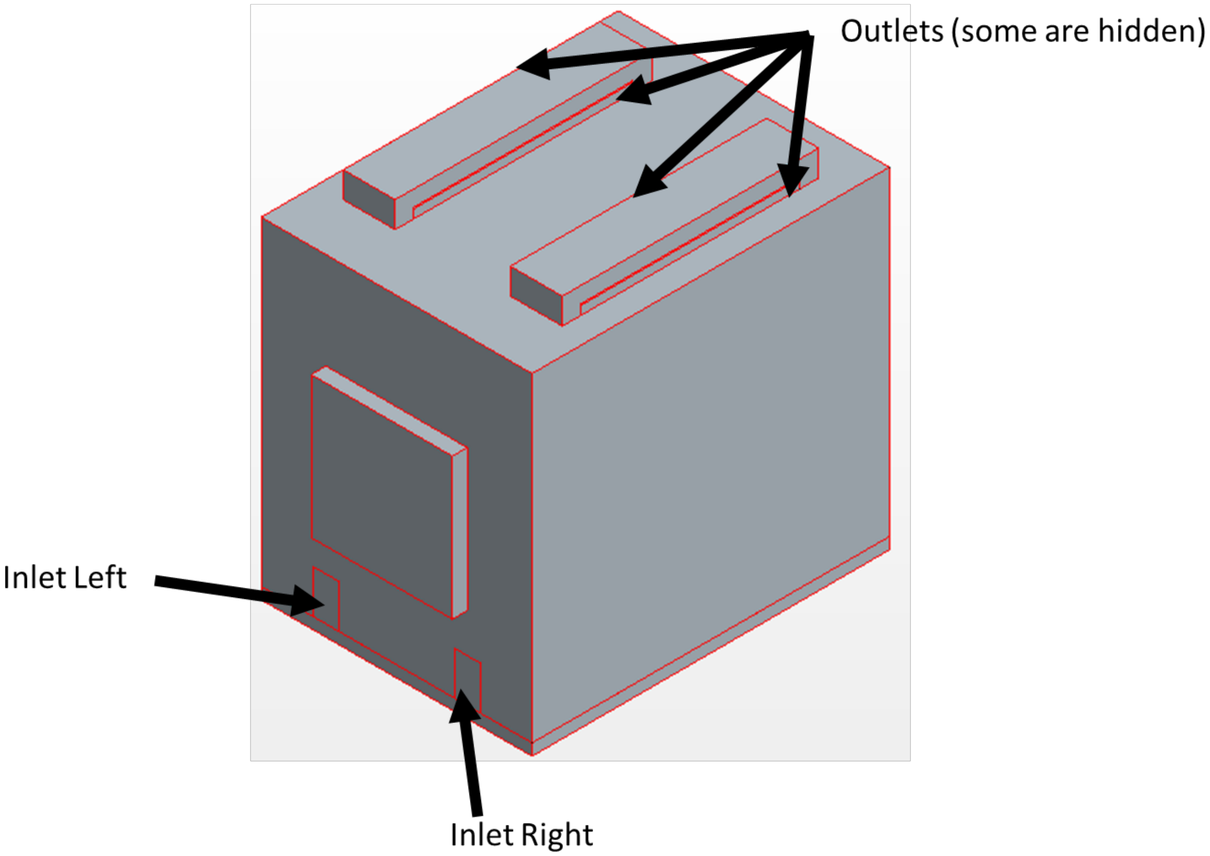

Figure 4-6. Diagram of the Inlets and Outlets on the AHSM-HS Single Module

Table 4.7. Thermal Response to Changing Wind Directions

Wind Direction[a] [deg.]	Max. Temp. Cladding [°C]	Max. Temp. Canister [°C]	Average Temp. Cladding [°C]	Average Temp. Canister [°C]
0	394	205	274	166
30	396	206	275	168
45	397	207	277	170
60	399	210	280	172
90	408	218	289	180
120	405	215	286	178
135	406	216	287	179
150	406	215	287	179
180	403	214	283	175

[a] 0° wind direction corresponds to the wind being normal to the inlets of the cask.

Table 4.8. Mass Flow Into (+) and Out of (-) the Cask.

Wind Direction[a] [deg.]	Mass Flow Inlet Left [kg/s]	Mass Flow Inlet Right [kg/s]	Mass Flow left Outlet [kg/s]	Mass Flow Right Outlet [kg/s]
0	0.75	0.75	-0.75	-0.75
30	0.70	0.68	-0.57	-0.81
45	0.62	0.62	-0.40	-0.84
60	0.60	0.51	-0.32	-0.79
90	0.33	0.33	-0.37	-0.33
120	0.36	0.42	-0.21	-0.56
135	0.38	0.42	-0.17	-0.60
150	0.35	0.43	-0.38	-0.36
180	0.44	0.44	-0.44	-0.43

[a] 0° wind direction corresponds to the wind being normal to the inlets of the cask.

5. CONCLUSION AND FUTURE INVESTIGATION

This investigation validated and verified several aspects of CFD modeling of environmental effects on ventilated spent nuclear fuel storage systems. The modeling effort with the BVDCS showed that STAR-CCM+ modeling of the entire system including external environment produced results that were representative of the wind effects experimental study in Durbin and Lindgren (2017). The results indicate that STAR-CCM+ can be used as a tool in creating accurate wind effects models of SNF dry storage systems with an external environment. This further contributes to effective use of STAR-CCM+ for investigating wind and particle deposition effects for the CDFD project. The investigation with the BVDCS identified a number of model improvements applicable to improving the CFD models utilized in the CDFD project. The solar radiation comparison in this study showed a clear method for implementing solar radiation into the wind effects models. These wind effects solar radiation models have been confirmed to represent the intended solar radiation loading. Also, further confirmation of the solar radiation models was achieved with the comparison to modeling performed using ANSYS APDL. This provides further support for using solar radiation models in STAR-CCM+. The final portion of this report reviewed previous studies and data from two NUHOMS® models, HSM-15 and AHSM-HS. The conclusion from this review showed similar flow and thermal response to the previous validation case using the BVDCS. In addition to this, further modeling efforts and improvements were identified for the AHSM-HS. This is important in providing further modeling support for the CDFD project.

From this study, several topics for future research were identified. These topics include continuation of the modeling efforts discussed earlier as well as new applications for wind effects in the context of modeling SNF dry storage systems. The main goal for future research is to apply the topics investigated in this report to full wind effects models of a SNF storage cask system. This report showed that the flow modeling of the wind effects model matches well with experimental data. The wind effects models will be integral to development of future particle deposition models. The wind effects models will provide a more realistic prediction of how many particles and what particle distribution would enter the overpacks. This information could then be fed into a standalone model and a more accurate prediction of canister deposition provided. Future wind effects modeling could also look at more site-specific models and how structures around the overpack impact the flow and particles entering the overpack. It is important to note that the PNNL deposition models are preliminary and will require further development, including validating the deposition model with small scale testing. Flow conditions, including those caused by wind, will be important to consider in small scale testing. Large scale testing planned in the CDFD project will also be used to validate the deposition models.

Future investigation will be primarily focused on improving the NUHOMS® AHSM-HS model for the CDFD project. In this report a limited set of cross wind data was available for the AHSM-HS, so one point for future research is to further extend this data set to better match those of the BVDCS and HSM-15. Providing additional comparison between these will provide greater understanding of the influence of wind on the AHSM-HS and will provide further verification that the model is behaving as expected.

An extensive mesh sensitivity analysis has not been performed on this wind effects AHSM-HS model. As shown in Section 2.2, the final solution (PCT temperature in this case) can be particularly sensitive to the meshing practices used. Certain areas of flow can be more influenced by the detail of the mesh used. For future investigation a mesh sensitivity study will be performed on the areas around the inlet and outlets of this cask system. A refined mesh in these areas can help better understand back flow from the outlets to inlets. Although for the limited wind speeds analyzed here for the AHSM-HS, no backflow was observed, it could be possible under other external flow conditions and mesh refinements. Also, better computational efficiency could be achieved with a mesh optimization study.

This effort utilized a single standalone module. The NUHOMS® AHSM-HS deployed in an ISFSI is paired with at least two other modules. An additional topic for future investigation is wind effects models utilizing three modules. An initial three module wind effects model was developed in Suffield et al. (2021) but has not been extensively analyzed for thermal and flow response.

Overall, this NUHOMS® AHSM-HS cask system shows similar cross wind response as the HSM-15 and BVDCS. This initial investigation revealed areas for further research and comparison. In addition to the specific topics discussed here, future work could be done to compare additional horizontal cask systems and vertical systems as well.

Additional areas in which future work could be focused are listed below:

- Further confirmatory validation with other CFD modeling software and exploration of different turbulence models such as large eddy simulation
- Expand to full-scale vertical storage module
- Environmental transients
- Off-normal conditions
- Sensitivity studies with emphasis on uncertainty analysis
- Determine conditions in which natural convection is dominated by wind driven flow

6. REFERENCES

10 CFR 71. “Packaging and Transportation of Radioactive Material,” *Code of Federal Regulations*, January 2020.

Adams BM, WJ Bohnhoff, KR Dalbey, MS Ebeida, JP Eddy, MS Eldred, RW Hooper, PD Hough, KT Hu, JD Jakeman, M Khalil, KA Maupin, JA Monschke, EM Ridgway, AA Rushdi, DT Seidl, JA Stephens, LP Swiler, , and JG Winokur. 2020. *Dakota, A Multilevel Parallel Object-Oriented Framework for Design Optimization, Parameter Estimation, Uncertainty Quantification, and Sensitivity Analysis: Version 6.12 User’s Manual*. SAND2020-12495, Sandia National Laboratories, Albuquerque, New Mexico.

ANSYS, Inc. 2016. “ANSYS Mechanical APDL 16.0”, ANSYS Inc. Canonsburg, Pennsylvania.

Calhoun, R., S. Chan, R. Lee, J. Leone, J. Shinn and D. Stevens, 2004. Flow around a complex building: Comparisons between experiments and a Reynolds-averaged Navier-Stokes approach. *J. Appl. Meteor.*, 43, 696-710.

Calhoun, R., F. Gouveia, J. Shinn, S. Chan, D. Stevens, R. Lee and J. Leone, 2005. Flow around a complex building: Experimental and large-eddy simulation comparisons. *J. Appl. Meteor.*, 43, 696-710.

Durbin SG and ER Lindgren. *Thermal-Hydraulic Results for the Boiling Water Reactor Dry Cask Simulator.* SAND2017-10551 R, Sandia National Laboratories, Albuquerque, New Mexico.

Durbin SG, ER Lindgren, SR Suffield and JA Fort. *Status Update for the Canister Deposition Field Demonstration*. SAND2021-6471 R, Sandia National Laboratories, Albuquerque, New Mexico.

Jensen PJ, SR Suffield, and BJ Jensen. 2020. *Status Update: Deposition Modeling For SNF Canister CISCC*. PNNL-30793. Pacific Northwest National Laboratory, Richland, Washington.

Jiang N, W Layton, M McLaughlin, Y Rong, and H Zhao. 2020. "On the Foundations of Eddy Viscosity Models of Turbulence," *Fluids* 5(4):167.

Kumar N, T Kubota, Y Tominaga, M Shirzadi, and R Bardhan. 2021. “CFD simulations of wind-induced ventilation in apartment buildings with vertical voids: Effects of pilotis and wind fin on ventilation performance.” *Build. Environ*. 194 (2021), https://doi.org/10.1016/j.buildenv.2021.107666.

Modi PP and S Jayanti. 2004. “Pressure Losses and Flow Maldistribution in Ducts with Sharp Bends.” *Chemical Engineering Research and Design* 82(A3):321-331.

Russo F and NT Basse. 2016. "Scaling of turbulence intensity for low-speed flow in smooth pipes." *Flow Measurement and Instrumentation* 52:101-114.

Siemens PLM Software. 2021. STAR-CCM+ 16.02 (computer software). Plano, Texas: Siemens PLM Software.

Solis, J and Zigh, A, “Impact of Variation in Environmental Conditions on the Thermal Performance of Dry Storage Casks,” NUREG-2174, Nuclear Regulatory Commission, Washington, D.C., February 2015.

Stern F, WV Wilson, HW Coleman, and EG Paterson. 2001. “Comprehensive Approach to Verification and Validation of CFD Simulations – Part 1: Methodology and Procedures.” *Journal of Fluids Engineering* 123(4):793-802. doi.org/10.1115/1.1412235.

Suffield, SR, JA Fort, HE Adkins, JM Cuta, BA Collins and ER Siciliano. 2012. *Thermal Modeling of NUHOMS® HSM-15 and HSM-1 Storage Modules at Calvert Cliffs Nuclear Power Station ISFSI*. PNNL-21788. Pacific Northwest National Laboratory, Richland, WA.

Suffield SR, DJ Richmond, and JA Fort. 2020a. *Modeling of the Boiling Water Reactor Dry Cask Simulator.* PNNL-28424, Rev. 1. Pacific Northwest National Laboratory, Richland, Washington.

Suffield SR, DJ Richmond, BJ Jensen, JA Fort, and C Grant. 2020b. *Modeling of the Horizontal Boiling Water Reactor Dry Cask Simulator.* PNNL-30145. Pacific Northwest National Laboratory, Richland, Washington.

Suffield SR, JA Fort, PJ Jensen, WA Perkins, BJ Jensen, C Grant, R Ekre, BD Hanson, and SB Ross. 2021. *Thermal and Deposition Modeling of the Canister Deposition Field Demonstration*. PNNL-31882, Pacific Northwest National Laboratory, Richland, Washington.

van Hooff T, B Blocken, and Y Tominaga. 2017. "On the accuracy of CFD simulations of cross-ventilation flows for a generic isolated building: Comparison of RANS, LES and experiments." *Build. Environ*. 114 (2017) 148–165, https://doi.org/10.1016/j.buildenv.2016.12.019.

United States Nuclear Regulatory Commission (NRC) 2020 Zigh A and S. Gonzalez. 2020. *Validation of a Computational Fluid Dynamics Method Using Vertical Dry Cask Simulator Data*. NUREG-2238. U.S Nuclear Regulatory Commission, Washington, D.C.